

Quantitative phase microscopies: accuracy comparison

Patrick C. Chaumet¹, Pierre Bon², Guillaume Maire¹, Anne Sentenac¹
and Guillaume Baffou^{1,3*}

¹Aix Marseille Univ, CNRS, Centrale Marseille, Institut Fresnel, Marseille, France.

²Université de Limoges, CNRS, XLIM, UMR 7252, F-87000 Limoges, France.

³Neurotechnology Center, Department of Biological Sciences, Columbia University, New York, NY 10027, USA.

Contributing authors: guillaume.baffou@fresnel.fr;

Abstract

Quantitative phase microscopies (QPMs) play a pivotal role in bio-imaging, offering unique insights that complement fluorescence imaging. They provide essential data on mass distribution and transport, inaccessible to fluorescence techniques. Additionally, QPMs are label-free, eliminating concerns of photobleaching and phototoxicity. However, navigating through the array of available QPM techniques can be complex, making it challenging to select the most suitable one for a particular application. This article presents a thorough comparison of the main QPM techniques, focusing on their accuracy in terms of measurement precision and trueness. We focus on 8 techniques, namely digital holographic microscopy (DHM), cross-grating wavefront microscopy (CGM), which is based on QLSI (quadrivave lateral shearing interferometry), diffraction phase microscopy (DPM), differential phase-contrast (DPC) microscopy, phase-shifting interferometry (PSI) imaging, Fourier phase microscopy (FPM), spatial light interference microscopy (SLIM), and transport-of-intensity equation (TIE) imaging. For this purpose, we used a home-made numerical toolbox based on discrete dipole approximation (IF-DDA). This toolbox is designed to compute the electromagnetic field at the sample plane of a microscope, irrespective of the object's complexity or the illumination conditions. We upgraded this toolbox to enable it to model any type of QPM, and to take into account shot noise. In a nutshell, the results show that DHM and PSI are inherently free from artefacts and rather suffer from coherent noise; In CGM, DPC, DPM and TIE, there is a trade off between precision and trueness, which can be balanced by varying one experimental parameter; FPM and SLIM suffer from inherent artefacts that cannot be discarded experimentally in most cases, making the techniques not quantitative especially for large objects covering a large part of the field of view, such as eukaryotic cells.

Keywords: Quantitative phase microscopy, wavefront microscopy, precision, accuracy, trueness, DDA, simulations

1 Introduction

Quantitative phase imaging (QPI) refers to a family of optical imaging techniques that aim at imaging the phase of a light beam [1–5], a quantity that is normally not accessible using common optical

sensors. QPI has witnessed remarkable progress these last 2 decades, fueled by advances in optical instrumentation and computing technology. QPI techniques have been heavily used in optical *microscopy*, leading to the closely-related field

of quantitative phase microscopy (QPM), and significantly expanded the capabilities of microscopy in cell biology. One of the main strength of QPM in cell biology is its ability to measure the dry mass of cells, due to the close relation that exists between refractive index and mass density [6–9]. The dry mass is defined as the mass of the cell excluding its water content, *i.e.*, the mass of biological material. Monitoring the dry mass of cells enables precise measurements of cellular growth rate and matter transport at the single cell level in a label-free, non-invasive manner.

The optical path difference (OPD) $\delta\ell$ map is the image that is often computed in practice, in QPM, rather than the phase image itself. It is defined by the optical path variation created by the imaged object once placed in the field of view of the microscope. It is simply related to the phase image φ *via* the relation

$$\varphi = \frac{2\pi}{\lambda} \delta\ell. \quad (1)$$

The interest of the OPD is that, in first approximation, it is directly proportional to the dry mass density ρ (pg/ μm^2) of live cells, in particular far from absorbing bands, :

$$\rho = \gamma^{-1} \delta\ell, \quad (2)$$

where γ is called the specific refraction increment. For biological media, it is approximately constant, ranging from 0.18 to 0.21 $\mu\text{m}^3/\text{pg}$. From the dry mass density can be computed the dry mass of the imaged cell by image segmentation and pixel summation.

Note that the dry mass is the most popular physical quantity that QPM can quantify in biology, but there exist other readouts of interest, as listed in Ref. [10], namely the optical volume, some phase/mass ratiometric quantities, sphericity/eccentricity indices, phase kurtosis and skewness. Also, more advanced tomography techniques can also measure cell volume and refractive index distribution in 3 dimensions.

QPM methods encompass a diverse array of techniques, developed since the late 90s. Most of them consist of making interfere several beams to transform the phase information into intensity variations, measurable using common optical sensors. Albeit numerous, common QPM techniques

can be classified into two main categories: *off-axis* techniques and *multiple-image* techniques.

The off-axis techniques consist of making interfere two (or more) light beams impinging on a camera, tilted by a small angle to each other, to create fringes that contain the phase information. The raw image, registered by the camera, is called an interferogram, and the related techniques are off-axis DHM (digital holographic microscopy) [11, 12], DPM (diffraction phase microscopy) [13] and CGM (cross-grating wavefront microscopy) [14, 15].

The multiple-image techniques consist in acquiring several successive images of the object of interest under different conditions. These images are then numerically mixed to derive the wavefront or phase profile. Among them, the phase-shifting techniques also consist of the interference between two beams, an object beam and a reference beam, but the two beams are collinear [16]. Thus, no interference pattern (no fringes) appears on the camera. When no tilt is applied between the two beams, no bijective relation exists between the grayscale intensity on each camera pixel, and the light phase. Intensity and phase can be retrieved separately by the acquisition of 4 images associated with 4 phase shifts of 0, $\pi/2$, π and $3\pi/2$ applied to one of the two beams. The related techniques are PSI (phase-shifting interferometry imaging) [16–19], FPM (Fourier phase microscopy) [20, 21] and SLIM (spatial light interference microscopy) [22]. There also exist non-interferometric techniques, where multiple bright-field images are acquired, *e.g.*, under various conditions. The related techniques are differential phase contrast (DPC) microscopy [23–25], which acquires 4 images of an object obtained with 4 different illumination angles, and combine the 4 images to retrieve the phase of the sample; and TIE (transport-of-intensity equation) microscopy, also called phase-diversity, which combines 3 different images at different focuses to reconstruct the wavefront profile [26].

Selecting the right QPM for a specific application is complex, as they all serve the same purpose. Review articles have been published, but they mainly aim at reviewing the applications [1–4], not really comparing the techniques with each other. Some articles and reviews recently aimed at comparing QPM techniques [5, 27, 28]. However, they

concern only few QPM techniques and are usually restricted to some particular types of objects.

The other issue we recently raised [15] is the presence of inconsistencies in the literature, where some QPMs render much different images of similar objects: Figure 1 displays neurons imaged using CGM, DPM and SLIM. While the images in Figs. 1(a) and 1(b) look consistent, featuring bumpy cell somas, the somas in images Figs. 1(d) and 1(e) look void. When noticing that a OPD image is supposed to represent the dry mass density, it becomes apparent that such images may not accurately reflect reality, as the cell soma contains much biological material. This raises questions about the level of accuracy achievable across QPM techniques.

In this article, we aim to compare the most commonly used QPM techniques, and in particular their relative degrees of accuracy, *i.e.* their precision and trueness. We focus on 8 QPM techniques, namely DHM, CGM/QLSI, FPM, DPM, PSI, SLIM and TIE. For the sake of comprehensiveness, we present results of numerical simulations arising from the modelling of each of the 8 microscopy setups. Our algorithm enables the computation of QPM images, including the noise amplitude and the possible presence of inherent artefacts. The first part introduces the working principles of the 8 techniques, recalls their experimental configuration, their theory and their image processing methods. The second part describes the numerical tool we developed and used to model each microscopy technique. Finally, results of numerical simulations are presented, on 4 model objects: a nanoparticle, a bacterium, a uniform slab (2D material), and a eukaryotic cell. The precision and trueness of each microscopy techniques are discussed and the origins of noise and inaccuracies are explained.

2 QPM techniques

This section describes the 8 QPM techniques investigated in this article, one by one, namely DHM, CGM/QLSI, DPM, DPC, FPM, PSI, SLIM and TIE. All these techniques involve a microscope, and a camera at the image plane. To describe the formalism, we shall consider monochromatic fields, using complex number notations, at the angular frequency ω , defining

the wavenumber $k = \omega/c$ and the wavelength $\lambda = 2\pi/k$.

This section only describes the working principles of the techniques. The advantages and limitations of each technique will be discussed in the following sections.

2.1 Bright-field microscopy

Let us first introduce the basic experimental system and the notations with the case of the bright-field microscope (4).

We consider an object standing in the object space of the microscope. This object is illuminated in transmission by the so-called incident light beam, resulting in the generation of a scattered electric field. Let us call E_0 the electric field at the *image* plane of a conventional microscope (no QPM for the moment) coming from the incident light, and E_s the electric field at the image plane scattered by the sample. The total electric field at the image plane reads thus, no matter the size and nature of the object and without approximation,

$$E(\mathbf{r}) = E_0(\mathbf{r}) + E_s(\mathbf{r}). \quad (3)$$

The quantity of interest in QPM is the phase φ of E , which is such that

$$E(\mathbf{r}) = A(\mathbf{r})e^{i\varphi(\mathbf{r})}, \quad (4)$$

where $A(\mathbf{r}) = |E(\mathbf{r})|$.

When detecting this field with a camera sensor, the measured quantity is $I = A^2$, cancelling any information on φ . The following sections describe how φ can nevertheless be retrieved using camera sensors.

Note that all the equations above assume a scalar electric field. This scalar approximation in optics is usually employed and valid in two cases: (i) with a linearly polarized illumination, where the scattered light is assumed to globally retain the incident polarisation, and (ii) with an unpolarized illumination, where the two components of the electric are likely to remain identical. However, in some cases, the scalar approximation is no longer valid, in particular when studying anisotropic particles or birefringent materials. The more general formalism involves two scalar fields,

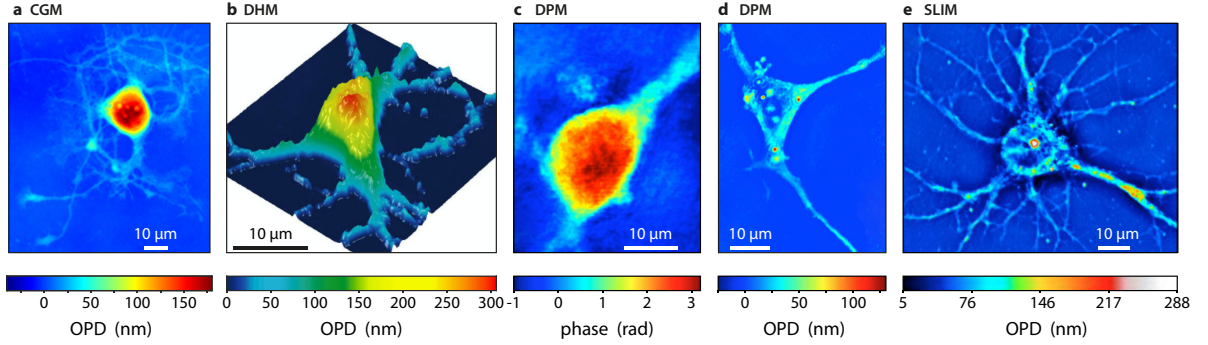


Fig. 1 OPD and phase images of neurons acquired using different techniques (a) OPD of a hippocampal neuron imaged using CGM/QLSI [29]. (b) OPD of a mouse cortical neuron imaged using DHM. Reprinted with permission from [11]. Copyright 2014 SPIE. (c) Phase image of a neuron imaged using DPM. Reprinted with permission from [13]. Copyright 2014 Optical Society of America. (d) OPD image of a neuron imaged using DPM. Reprinted with permission from [30]. Copyright 2018 Wiley. (e) OPD of a hippocampal neuron imaged using SLIM. Reprinted with permission from [22]. Copyright 2011 Optical Society of America.

corresponding to the x and y components of the electric field, and Eqs. (3) and (4) becomes more generally:

$$\mathbf{E}(\mathbf{r}) = \mathbf{E}_0(\mathbf{r}) + \mathbf{E}_s(\mathbf{r}), \quad (5)$$

$$\mathbf{E}(\mathbf{r}) = A_x(\mathbf{r})e^{i\varphi_x(\mathbf{r})}\mathbf{u}_x + A_y(\mathbf{r})e^{i\varphi_y(\mathbf{r})}\mathbf{u}_y. \quad (6)$$

The concept of "the phase of a light beam" is therefore ambiguous in the most general case. There are in principle 2 phase profiles. In the following sections, when describing the theory of each QPM, we will consider the scalar approximation, for the sake of simplicity.

2.2 Off-axis techniques

Off-axis techniques involve the interference of multiple waves, which create fringes on the camera sensor. These fringes are processed using a demodulation algorithm to retrieve the phase or wavefront of the light beam. This family includes DHM, CGM, and DPM.

2.2.1 Digital holographic microscopy (DHM)

The most common QPM method is off-axis digital holographic microscopy (DHM) [11, 12]. It consists of a coherent plane wave E_{ref} sent on the camera sensor at a tilted angle θ (Fig. 2(c)), in addition to the object beam characterized by an electric field E . The overlap of tilted illuminations is usually created with a Mach-Zehnder

interferometry configuration. The resulting interference pattern measured by the camera, called the interferogram, consists of fringes and reads

$$\begin{aligned} I &= |E + E_{\text{ref}}|^2 \\ I &= |E|^2 + |E_{\text{ref}}|^2 + 2|E||E_{\text{ref}}|\cos(k_x x + \varphi), \end{aligned} \quad (7)$$

where $k_x = k \sin \theta$. The phase map can be extracted by a demodulation of the interferogram image using a Fourier-transform-based algorithm [32].

2.2.2 Cross-grating wavefront microscopy

Cross-grating wavefront microscopy (CGM) is a microscopy technique based on the wavefront imaging technique called quadriwave lateral shearing interferometry (QLSI), invented and patented by Primot *et al.* in 2000 [33, 34]. CGM consists of implementing a QLSI camera in the image plane of an optical microscope (Fig. 2(b)) [14, 15]. A QLSI camera is composed of a 2-dimensional diffraction grating placed at a millimeter distance from a camera sensor. A QLSI grating is designed such that it diffracts only the 1st orders, creating 4 replicas of the image, separated by a distance a on the camera sensor [35]. Because the 4 waves impinging on the camera are not only shifted but also tilted by the grating, by an angle θ , fringes appear, just like in off-axis DHM. For the sake of simplicity and understanding in this paper, let us consider the interference pattern obtained from

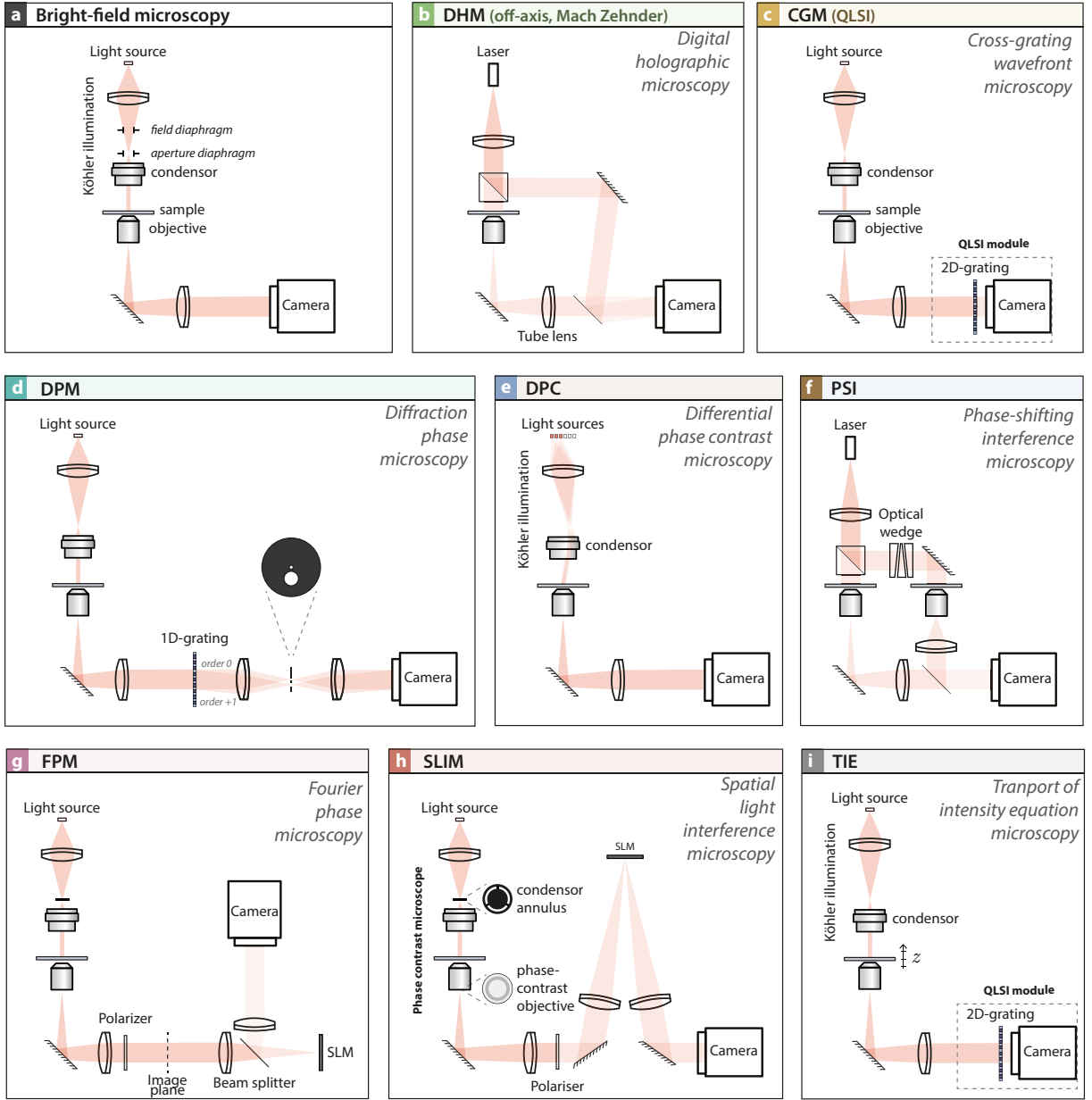


Fig. 2 Schematics of the QPM experimental setups investigated in this study. (a) Bright-field microscopy. (b) Digital holographic microscopy (DHM), an off-axis QPM technique, involving a reference arm. (c) Cross-grating wavefront microscopy (CGM), a technique based on the use of a 2D diffraction grating placed at a millimeter distance from a camera (an association called quadriwave lateral shearing interferometry (QLSI)). (d) Diffraction phase microscopy (DPM), an off-axis QPM based on the use of a 1D-diffraction grating placed in the image plane of the microscope, and a mask placed in the Fourier plane. (e) Differential phase-contrast (DPC) microscopy, based on the use of a series of tilted illuminations. (f) Phase-shifting interferometry (PSI), the standard phase-shifting imaging technique. (g) Fourier Phase microscopy (FPM) and (h) spatial light interference microscopy (SLIM), which are phase-shifting techniques using a spatial light modulator (SLM). (i) Transport of intensity equation (TIE) microscopy, based on the acquisition of various images acquired at various focuses. All the setups are shown in transmission because it is more common, but reflection configurations also exist [31].

only 2 replicas on the camera sensor, instead of 4: [15]:

$$I = |E(x + a/2)e^{ik_x x} + E(x - a/2)e^{-ik_x x}|^2$$

$$I = I_1 + I_2 \cos\left(\frac{4\pi}{\Gamma}x + d\nabla_x W\right), \quad (8)$$

where W is the wavefront profile, $k_x = k \sin \theta$, I_1 and I_2 are the intensity components, Γ is the pitch of the grating (grixel size) and d is the grating/camera distance. The 4-beam interference equation can be found in the literature [14].

Using a very similar algorithm as off-axis DHM, not the phase information but the wavefront gradients, along x and y , can be retrieved by two demodulations in the Fourier space [35, 36]. The wavefront profile W can then be retrieved from its two gradients by numerical integration.

Note that the wavefront profile directly equals the OPD,

$$W = \delta\ell, \quad (9)$$

meaning that one does not need to convert the phase into the OPD like with other QPM techniques. In CGM/QLSI, the measured quantity is directly the quantity of interest in cell biology, proportional to the dry mass density (Eq. (2)).

QLSI is not the only technique that is based on the positioning of an optical element at the vicinity of a camera, as a means to gain more information than $|\mathbf{E}|^2$. In particular, a microlens arrays [37, 38] or a diffusing plate [39] can also be placed at the vicinity of a camera. Diffuser-based phase sensing and imaging (DIPSI) uses a simple thin diffuser to retrieve the wavefront profile of a light beam [39], with a slightly reduced spatial resolution compared with QLSI. Shack-Hartmann (SH) wavefront imaging uses an array of microlenses to recover a wavefront profile [37, 40]. The spatial resolution is even lower than QLSI or DIPSI, making SH imaging rarely used in microscopy [41]. Light field microscopy (LFM) also uses an array of microlenses, but to retrieve another hidden information: the angular distribution of the light impinging at the sensor plane [38, 42]. We propose to refer to these techniques as *sensor-proximity* techniques, *i.e.* techniques that place an optical element close to the camera sensor that redistributes the light intensity profile to reveal hidden information. Information theory says that

if we gain information somewhere, we should also lose some information elsewhere. Indeed, with this technique family, this gain in information is accompanied by a loss in image definition.

2.2.3 Diffraction phase microscopy (DPM)

In diffraction phase microscopy (DPM), the camera is replaced by a 1-dimensional diffraction grating (Fig. 2(d)) [13] optically conjugated by a 4- f system on the camera, placed further along the optical axis. The Fourier plane of this system can be experimentally accessed within the 4- f system, where a transmission mask is implemented. This mask, composed of two holes, cuts any light but the zero-order spot and one of the 1st-order diffraction spots. Importantly, the diameter of the hole cropping the zero-order has to be small enough to act as a low-pass filter to transform the transmitted light into a plane wave, acting as the reference beam just like in DHM. At the image plane of the 4- f system, where the camera is positioned, one beam is coming from the 1st order, representing the image impinging on the camera with a tilt angle, and another beam is coming from the zero-order, acting as a reference plane wave. The retrieval algorithm is thus exactly the same as in DHM (Eq. (7)). DPM is called a common-path QPM technique, because no external reference arm exists. Here lies the interest of DPM and common-path techniques, discarding a separate reference arm that is a source of instabilities.

2.3 Illumination-based differential phase contrast (DPC)

DPC is based on the sequential acquisition of a set of intensity images, using a standard bright field microscope, with various illumination conditions. For this purpose, a DPC microscope involves a large numerical aperture in illumination (typically 0.4, or even less), created by an extended source of light located in the front focal plane of the condenser (or far enough from the sample in the case there is no Köhler illumination) [23]. This extended source is uniformly switched on in the case of bright field microscopy (Fig. 2(a)). In the case of DPC, the light source is cut into two parts about its center, named left and right

(Fig. 2(e)). Each half of the illumination gives rise to an asymmetric illumination. The two corresponding images, I_{left} and I_{right} , are acquired. Then, the light source is split about the orthogonal axis to generate two other illuminations and two new images that we name I_{top} and I_{bottom} . This set of 4 images are used to generate the DPC images defined by [23]

$$I_1^{\text{DPC}} = \frac{I_{\text{top}} - I_{\text{bottom}}}{I_{\text{top}} + I_{\text{bottom}}}, \quad (10)$$

$$I_2^{\text{DPC}} = \frac{I_{\text{right}} - I_{\text{left}}}{I_{\text{right}} + I_{\text{left}}}. \quad (11)$$

The basic idea of DPC is that these image subtractions contain information on the phase gradient, respectively along x and y directions. To demonstrate this relation, an important assumption needs to be made. First, one needs to consider the object as a plane of transmittance $t(x, y) = \exp(-\mu(x, y) + i\phi(x, y))$, where ϕ is the phase image of interest, to be determined. Then, μ and ϕ have to be small enough so that

$$t \approx 1 - \mu + i\phi. \quad (12)$$

This approximation also neglects any cross term between μ and ϕ . In this condition, one can define some point-spread-functions in intensity and phase, namely H_{abs} and H_{pha} so that the intensity at the camera plane I can be expressed using convolutions:

$$I = B + H_{\text{abs}} * \mu + H_{\text{pha}} * \phi, \quad (13)$$

where B is a uniform image, corresponding to the average intensity and $*$ denotes the convolution product. H_{abs} and H_{pha} are like point-spread-functions (PSFs) in intensity and phase. In this expression, only the last (phase) term depends on the illumination side (right or left, top or bottom). Here lies the interest of considering the image subtraction introduced above (Eqs. (10)), which become:

$$I_1^{\text{DPC}} = \frac{(H_{\text{pha}}^{\text{top}} - H_{\text{pha}}^{\text{bottom}}) * \phi}{I_{\text{top}} + I_{\text{bottom}}}, \quad (14)$$

$$I_2^{\text{DPC}} = \frac{(H_{\text{pha}}^{\text{right}} - H_{\text{pha}}^{\text{left}}) * \phi}{I_{\text{right}} + I_{\text{left}}}. \quad (15)$$

Note that the denominators of the two right-hand sides of the equation are supposed to be both equal to the bright field image. ϕ , the quantity of interest, is then retrieved by a deconvolution algorithm based on Fourier transforms and a Tikhonov's regularization:

$$\phi = \mathcal{F}^{-1} \left[\frac{\sum_j \tilde{H}_j^* \tilde{I}_j^{\text{DPC}}}{\sum_j |\tilde{H}_j|^2 + \epsilon} \right], \quad (16)$$

with $H_1 = (H_{\text{pha}}^{\text{top}} - H_{\text{pha}}^{\text{bottom}})/B$, $H_2 = (H_{\text{pha}}^{\text{right}} - H_{\text{pha}}^{\text{left}})/B$, where \tilde{A} denotes the Fourier transform of A : $\tilde{A} = \mathcal{F}(A)$ and \mathcal{F}^{-1} is the inverse Fourier transform. $\epsilon \ll 1$ is the Tikhonov regularization parameter. Decreasing its value gives more accurate results but increases the noise level. $\epsilon = 10^{-3}$ is considered as a good compromise [23, 43]. ϵ is the important degree of freedom to consider in DPC, as it significantly affects the accuracy of the measurements, as explained hereinafter.

2.4 Phase-shifting techniques

With phase-shifting QPM techniques, two beams interfere at the image plane, but without tilt. They propagate collinearly so that no fringe pattern is produced. This approach, which looks more natural and simpler than the off-axis approach, does not offer the possibility to retrieve the phase from a single image acquisition. The missing information can be retrieved by acquiring 4 images with $0, \pi/2, \pi$ and $3\pi/2$ overall phase shifts applied to one of the two beams. Only with such 4 images can the phase profile be reconstructed. In the following, we described the 3 phase-shifting techniques presented in this article, namely PSI, FPM and SLIM.

2.4.1 Phase-shifting interferometry (PSI) microscopy

PSI is an old technique [1, 16–19]. In PSI, a reference plane wave E_{ref} is overlapped with the wave crossing the object plane (Fig. 2(f)), just like in DHM (Fig. 2(c)). However, no tilt is applied so that the total intensity reads

$$\begin{aligned} I(\mathbf{r}) &= |E(\mathbf{r}) + E_{\text{ref}}|^2 \\ I(\mathbf{r}) &= |E(\mathbf{r})|^2 + |E_{\text{ref}}|^2 \\ &\quad + 2|E(\mathbf{r})||E_{\text{ref}}| \cos \varphi(\mathbf{r}). \end{aligned} \quad (17)$$

The issue with Eq. (17) is that the phase φ can no longer be retrieved from a demodulation around a carrier spatial frequency. There is no bijective relation between I and φ in Eq. (17), because I also depends on $|E|$, which is usually non-uniform.

To lift this limitation, not one, but 4 images are acquired, $I_{j \in \llbracket 0, 3 \rrbracket}$, corresponding to 4 different overall phase shifts ϕ_j between the object and reference fields, namely $0, \pi/2, \pi$ and $3\pi/2$:

$$\begin{aligned} I_j(\mathbf{r}) &= |E(\mathbf{r}) + E_{\text{ref}} \exp(i\phi_j)|^2 \\ I_j(\mathbf{r}) &= |E(\mathbf{r})|^2 + |E_{\text{ref}}|^2 \\ &\quad + 2|E(\mathbf{r})||E_{\text{ref}}| \cos(\varphi(\mathbf{r}) - \phi_j), \end{aligned} \quad (18)$$

where $\phi_j = j\pi/2, j \in \llbracket 0, 3 \rrbracket$.

The four images I_j enable the retrieval of the phase map φ using the simple expression [18]:

$$\varphi = \arg [(I_0 - I_2) + i(I_1 - I_3)]. \quad (19)$$

2.4.2 Fourier phase microscopy (FPM)

FPM is a phase-shifting technique that does not involve an external reference beam [20, 21]. This common-path technique only requires a simple plane wave illumination of the sample via a coherent light source, or a well-adjusted Köhler device, making this technique adaptable to any optical microscope without modifying it. Moreover, as a common-path technique, no temporal coherence is required and incoherent light sources can be used a priori. The two beams that interfere with artificial phase shifts are no longer E and E_{ref} , but E_0 and E_s , *i.e.*, the incident and scattered fields (see Eq. (3)). By varying the phase-shift ϕ_j between E_0 and E_s (see below), multiple images I_j can be obtained:

$$\begin{aligned} I_j(\mathbf{r}) &= |E_0 \exp(i\phi_j) + E_s(\mathbf{r})|^2 \\ I_j(\mathbf{r}) &= |E_0|^2 + |E_s(\mathbf{r})|^2 \\ &\quad + 2|E_s(\mathbf{r})||E_0| \cos(\varphi_s(\mathbf{r}) - \phi_j). \end{aligned} \quad (20)$$

Then, Eq. (19) is used to retrieve φ_s :

$$\varphi_s = \arg [(I_0 - I_2) + i(I_1 - I_3)]. \quad (21)$$

However, φ_s is the phase map of the scattered field E_s , not the phase map φ of the total field E . With FPM, one needs another step to retrieve

φ compared with PSI, which is given by this expression:

$$\varphi(\mathbf{r}) = \arctan \left(\frac{\beta(\mathbf{r}) \sin \varphi_s(\mathbf{r})}{1 + \beta(\mathbf{r}) \cos \varphi_s(\mathbf{r})} \right), \quad (22)$$

where the β image is defined by $\beta = |E_s/E_0|$ and can also be calculated from the 4 I_j images:

$$\beta = \frac{1}{4E_0} \frac{I_0 - I_2 + I_3 - I_1}{\sin(\varphi_s) + \cos(\varphi_s)}. \quad (23)$$

Experimentally, while it was straightforward to specifically apply the 4 phase shifts on the reference beam in PSI, one has here to apply the phase shifts only to the scattered field E_s , which is challenging because E_s and E_0 follow the same path. The assumption in FPM is to consider these two fields separated in the Fourier plane of the microscope. Indeed, the center of the Fourier space is where the light from E_0 is focused while the rest of the Fourier space contains only information related to the scattered field E_s . Thus, it suffices to apply a phase mask over a tiny area at the center of the Fourier plane to specifically apply the ϕ_j shifts to E_0 , which is performed using a spatial light modulator (SLM) conjugated with the back focal plane of the objective (Fig. 2(g)). One will see in this article that this assumption is not always valid because some scattered field can be contained within the central spot of the Fourier plane, in some cases. Moreover, the use of an SLM demands the use of a linearly polarised light beam.

2.4.3 Spatial light interference microscopy (SLIM)

SLIM [22] works exactly like FPM. There is just a slight difference with the experimental implementation. SLIM is meant to be adapted on a Zernike phase contrast (PC) microscope, involving a ring-like illumination and a special objective lens containing an annular phase mask. The annular mask of the objective is aimed to apply a phase shift of $\pi/2$ to the incident light field. The idea of SLIM is that PC microscopy can become quantitative if the phase shift of the annular mask could be varied and successively set to 4 values, to turn it into a phase-shifting technique. This is made possible by conjugating an SLM to the back focal plane of a PC microscope, applying annular

phase shifts matching the geometry of the phase mask of the objective lens. Moreover, to avoid losing too much intensity with a beam splitter, SLIM benefits from a slightly shifted beam propagation before and after the SLM (Fig. 2(h)). Here again, we shall see hereinafter than considering that the annulus contains only information related to the incident light beam E_0 is too strong an approximation in most cases.

2.5 Transport-of-intensity equation (TIE) microscopy

TIE microscopy only requires a normal bright-field microscope. The wavefront information can be retrieved using a set 3 images captured at 3 different focuses of the sample z (Fig. 2(f)). Here is the wavefront retrieval procedure.

From the Helmholtz equation governing the propagation of a light wave $A(\mathbf{r})e^{i\varphi(\mathbf{r})}$, one can derive the so-called transport-of-intensity equation (TIE), which no longer involves the electric field amplitude A , but the light intensity $I = A^2$ [26]:

$$\nabla_{\perp} \cdot [I(\mathbf{r})\nabla_{\perp} W(\mathbf{r})] = -\partial_z I(\mathbf{r}). \quad (24)$$

This equation is approximate, assuming that the light wave is a perturbation from a plane wave travelling along z . This equation tells how the transverse gradient of a light beam affects the variations of the intensity along the propagation axis. Assuming I and $\partial_z I$ are known, this equation has a unique solution for the wavefront profile W , provided that $I > 0$ everywhere in the image plane. To solve this equation, several methods exist. We use here the method proposed by Teague [26, 44], who showed that the vector field $I(\mathbf{r})\nabla_{\perp} W(\mathbf{r})$ derives from a scalar potential V :

$$I(\mathbf{r})\nabla_{\perp} W(\mathbf{r}) = \nabla_{\perp} V(\mathbf{r}). \quad (25)$$

Injecting this expression in Eq. (24) gives

$$\nabla_{\perp}^2 V(\mathbf{r}) = -\partial_z I(\mathbf{r}). \quad (26)$$

This equation in V can be solved using a Green's function formalism [44], or a Fourier transform formalism [26], which is the approach depicted below. The calculation of the gradient of a function can

be performed using Fourier transforms:

$$\nabla_{\perp} f(x, y) = i\mathbf{u}_x \mathcal{F}^{-1} [q_x \mathcal{F} [f(x, y)]] \quad (27)$$

$$+ i\mathbf{u}_y \mathcal{F}^{-1} [q_y \mathcal{F} [f(x, y)]] , \quad (28)$$

where $q_{x,y}$ are the variables conjugate to x and y in the Fourier space. Using this transformation, Eq. (26) can be solved

$$V(\mathbf{r}) = \mathcal{F}^{-1} [q^{-2} \mathcal{F} [\partial_z I(\mathbf{r})]] , \quad (29)$$

where $q^2 = q_x^2 + q_y^2$. Finally, injecting this expression of V in Eq. (25) gives

$$W(\mathbf{r}) = -\mathcal{F}^{-1} [q^{-2} \mathcal{F} [\nabla_{\perp} \cdot (I(\mathbf{r})^{-1} \nabla_{\perp} V(\mathbf{r}))]] . \quad (30)$$

In practice, in TIE microscopy, a conventional wide-field, transmission microscope is used. Three intensity images are acquired at 3 different focuses $z = 0, -\Delta z$, and Δz . Let us name them respectively I_0 , I_d , and I_u . The out-of-focus intensity images enable the estimation of the image of the intensity z -gradient, at $z = 0$:

$$\partial_z I = (I_u - I_d)/2\Delta z. \quad (31)$$

This image is used to compute V using Eq. (29), and then I_0 is used in Eq. (30) to compute the wavefront profile W . Note that with this approach, the intensity image is directly measured and given by I_0 , without image processing, unlike with CGM/QLSI or DHM, for instance, that require a demodulation, implying a loss in image definition (*i.e.* number of pixels).

2.6 Comparison of the QPM setups

Figure 3 summarizes the 8 QPM techniques presented in this study, their relationship to QPM categories (off-axis, multiple-image, phase-shifting, etc). Some features are also listed (number of images, degrees of freedom, etc).

Some techniques require the use of a coherent source of light (*i.e.* a cw laser), in particular with techniques that use a reference arm that do not necessarily have the same length as the main arm (not common-path techniques), such as DHM or PSI. Although interferences are involved in CGM/QLSI, DPM, FPM and SLIM, these techniques do not need the use of coherent light sources because the beam path is the

	DHM	CGM	DPM	DPC	PSI	FPM	SLIM	TIE
Measurement	phase	wave front	phase	phase	phase	phase	phase	wave front
Off-axis	●	●	●					
Multiple-image				●	●	●	●	●
Phase-shifting					●	●	●	
Sensor proximity		●						
Illumination-based				●				
Common-path		●	●	●		●	●	●
Coherent source	●				●			
# of images	1	1	1	4	4	4	4	3
# deg. of freedom	0	1	1	0	0	1	0	1
Transmittance (%)	50	44	~25	100	50	25	25	100
<p>DHM Off-axis digital holographic microscopy CGM Cross-grating wavefront microscopy (using QLSI) DPM Diffraction phase microscopy DPC Differential phase contrast microscopy PSI Phase shifting interferometry microscopy FPM Fourier phase microscopy SLIM Spatial light interference microscopy TIE Transport of intensity equation microscopy</p>								

Fig. 3 Technical features of the QPM techniques presented in this study, namely what they measure (wavefront or phase), their category (off-axis, phase-shifting, phase-diversity, or common-path), if they require a coherent source of light (*i.e.* cw laser illumination), the typical number of images required to form a phase/wavefront image, the number of experimental degrees of freedom, and the transmittance of the setup. The list of the abbreviations and their meanings are give below the table.

same between the different beams interfering at the image plane.

Figure 3 also displays the number of images that need to be acquired to construct the phase/wavefront images. The higher this number, the slower the technique. In PSI, FPM and SLIM, although 3 images would be sufficient in theory, 4 images are usually acquired to substantially improve the signal-to-noise ratio.

Some QPM techniques possess a degree of freedom (DoF) that can be adjusted experimentally. In CGM/QLSI, it is the grating-camera distance. In DPM, the DoF is the diameter of the 0-order hole in the mask. In DPC, the numerical aperture of the illumination has to match the NA of the objective lens, so the DoF is not really a DoF. DPC rather possesses a *numerical* DoF, which

is the Tikhonov regularization parameter α , and which can affect both the trueness and precision of the measurements. In FPM, the DoF is the diameter of the disc area on the SLM that phase-shifts the central part of the Fourier space. In TIE, the DoF is the defocus z between successive acquired images. As will be explained later, these DoFs are associated with a trade-off between trueness and precision.

The last line of this table corresponds to the optical transmission of the QPM techniques, defined as the t/t_0 where t is the percentage of photons reaching the camera compared with the number of photons impinging on the field of view of the microscope, and t_0 is t for a standard, bright-field transmission microscope (see Fig. 2). For CGM/QLSI, the transmission is the one of the grating, in which the opaque lines cover 5/9 of the area, leading to a transmission of 44%. DHM loses 50% due to the beam splitter. DPM loses 50% because of the opaque lines of the diffraction grating, and several 10% more due to the pinhole. PSI loses 50% because of the beam splitter. FPM transmission is 25% because the signal passes twice through a beam splitter. The transmission of SLIM is 50% because of the use of a linear polarizer to ensure a linear polarisation on the SLM [45], and 50% more because the phase mask in a phase-contrast objective lens usually also absorbs 50% of the intensity to improve the contrast. The transmission of DPC and TIE is 100% because they use a conventional bright-field microscope, with no additional optical element.

3 Numerical simulations using IF-DDA

Comparing 8 different experimental techniques with each other would have been cumbersome experimentally. Some articles experimentally compare several QPM techniques, but never more than 3 techniques [27, 28, 46], and not always on the same microscope with the same cameras, and sometimes not even using the same magnifications and numerical apertures [28], making any objective comparison complicated.

Here, we rather chose to *numerically* compare QPM techniques, so that we are not limited

by the number of techniques, and we can compare them on strictly equivalent microscopes, on strictly identical objects.

The numerical tool we use to model the microscopy techniques is based on the discrete dipole approximation (DDA) method, a common approach for electromagnetism simulations [47]. DDA algorithms require the meshing of only the object, not of the surrounding medium, and can easily take into account the presence of a flat interface (on which the sample is lying) [48]. We recently released a home-made DDA toolbox called IFDDA (for Institut-Fresnel or Idiot-Friendly DDA) [49, 50], which not only models the interaction between a light beam and an object, but also computes the image of this object by a microscope [49, 51], *i.e.*, the electromagnetic field at the image plane. It should be noted that all the calculations performed by the IFDDA code are made without any approximation within the vectorial framework.

In all numerical simulations, the incident illumination took the form of a plane wave or a superposition of plane waves, characterized by intensity, polarization (linear or circular), direction (not necessarily at normal incidence), and wavelength. The modeled microscope in all simulations involved a $100\times$ magnification, 1.3 NA objective lens, and a camera with a pixel size of $6.5\text{ }\mu\text{m}$ and a full-well-capacity of 25,000. The only exceptions were the use of a $60\times$ magnification exclusively for the neuron, and a 0.4 NA objective only for DPC simulations.

The program returns the vectorial electric field of the light at the image plane \mathbf{E} , being composed of the incident light \mathbf{E}_0 and the light scattered by the object \mathbf{E}_s (Eq. (3)). From \mathbf{E} , we compute the theoretical intensity $I_{\text{th}} = |\mathbf{E}|^2$, phase φ_{th} and wavefront W_{th} images at the image plane of a conventional (bright-field) microscope (see upper part of Fig. 4).

While computing I_{th} from \mathbf{E} is straightforward, computing φ_{th} or W_{th} is less obvious. First, as explained above, computing the phase and wavefront profiles of an electromagnetic field is not straightforward when taking into account polarisation: There are actually two phase maps, one for each transverse component of the light beam:

$$\varphi_x = \arg(E_x) \quad (32)$$

$$\varphi_y = \arg(E_y). \quad (33)$$

In all the simulations we conducted, the scalar approximation is supposed to remain valid, because none of the objects are birefringent. Nevertheless, in the simulations, we consider that the true phase map equals the average of these two profiles, weighted by the intensity maps:

$$\varphi_{\text{th}} = \frac{I_x \varphi_x + I_y \varphi_y}{I_x + I_y}. \quad (34)$$

This expression was derived in the case of CGM experiments [52], and we used it in this study for any QPM to determine the true phase profiles φ_{th} , and to compute $W_{\text{th}} = \varphi_{\text{th}} \lambda / 2\pi$.

In practice, φ_{th} can sometimes exceeds variations of 2π . In that case, an unwrapping algorithm is necessary. For the simulations presented in this study, we did not need to use unwrapping algorithms, because all the objects were not optically thick enough.

In QPM, this initial electromagnetic field \mathbf{E} , originally impinging on the camera in bright field microscopy, is transformed by optical elements, such as gratings, masks, and polarizers. To conduct the simulations presented in this article, we upgraded the IF-DDA toolbox so that it no longer computes only \mathbf{E} , but also the transformations generated by any QPM. More precisely, we modeled all the optical elements for each QPM technique (gratings, polarizers, and masks), and computed the resulting electric field at the camera plane. The numerical procedures for all the QPMs are sketched in Fig. 4. The codes of IF-DDA and of the QPM add-on are provided on public repositories [50]. This way, one can compute the raw image recorded by the camera for each QPM, and process it to get the phase image φ or wavefront image W using experimental processing algorithms, as if it were an actual experimental image. We can then compare the *true* maps, I_{th} , φ_{th} and W_{th} , at the image plane and calculated using IF-DDA, with the so-called *modelled* maps I , φ , and W obtained by post-processing the raw image captured by the camera, for each specific QPM. This way, any inaccuracy inherent to the working principle of QPM techniques can be evidenced, quantified and compared.

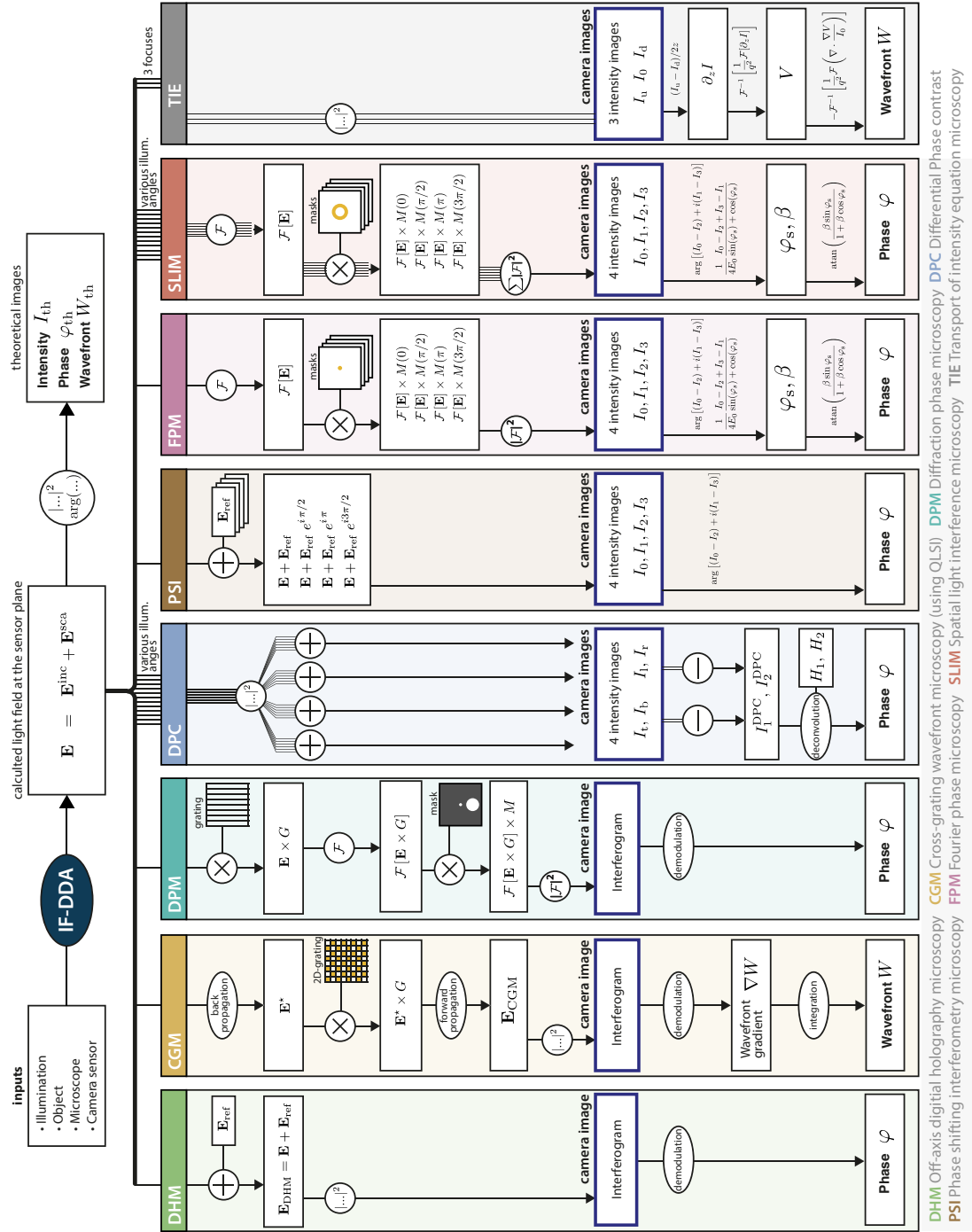


Fig. 4 Computing chart of *in silico* quantitative phase microscopies using IF-DDA. This chart shows the numerical procedure, starting from the computation of the light field at the sample plane of the microscope, and its processing using 8 different QPM microscope models, until the computation of the experimental-like intensity, phase, and wavefront images. These modelled images are aimed to be compared with the theoretical intensity, phase, and wavefront images directly calculated from the theoretical light field, as a means to evidence inherent artefacts of specific QPM, or quantify the noise amplitude on the modelled images, coming from the shot noise on the camera sensor.

For the techniques requiring a laser illumination or a linearly polarized illumination (see Fig. 3), we used a linearly polarized illumination. For the techniques using incoherent illumination, we used a circularly polarized illumination, to equally distribute the energy over the different polarisation axes.

Moreover, in the second part of our study, we numerically affected the raw camera image with shot noise as a means to quantify and compare the signal-to-noise ratios and precision of all the QPM techniques, assuming they are shot-noise limited. We neglect here other sources of noise, such as coherent noise (also called speckle noise), thermal and dark current noise.

Here are more details on this *in silico* experimental approach, the algorithms of which are sketched in Fig. 4, technique by technique.

3.1 CGM

To model CGM, we use the *in silico* procedure that we recently used and detailed in Ref. [53]. Briefly, we consider a circularly-polarised light beam impinging on the object at the sample plane at normal incidence, and compute the resulting electric field \mathbf{E} at the image plane using IF-DDA.

Then, we back-propagate \mathbf{E} using a Fourier-transform algorithm the grating-camera distance d . We multiply the back-propagated field by the complex transmittance of a QLSI grating, rotated by an angle of 53° around the optical axis (Oz) (to minimize Moiré effects), and then forward-propagate over the same distance d to get the interferogram recorded by the camera. Finally, we use an experimental processing algorithm to compute the intensity I and wavefront image W from the interferogram. Importantly, since CGM is not measuring a phase, but a wavefront gradient that is subsequently integrated, no unwrapping algorithm needs to be used in CGM. A CGM algorithm does not yield discontinuities on the phase/wavefront maps. The related Matlab code of this specific algorithm is provided on GitHub [36, 54].

3.2 DHM

To model DHM, we consider a linearly- x -polarised light beam impinging on the object at the sample plane at normal incidence, and compute the

resulting electric field \mathbf{E} at the image plane using IF-DDA. Then, at the image plane, we add the reference beam, as a linearly polarised plane wave tilted by an angle θ around the (Ox) axis: $\mathbf{E}_{\text{ref}} = E_{\text{ref}} \exp(i\mathbf{k} \cdot \mathbf{r})\mathbf{u}_x$ where $\mathbf{k} = (0, k \sin \theta, k \cos \theta)$. The intensity recorded by the camera is then simply calculated as

$$I = |\mathbf{E} + \mathbf{E}_{\text{ref}}|^2. \quad (35)$$

Then, the intensity map I is processed using a DHM algorithm, as if it were an experimental image, to compute the *modelled* phase map φ .

3.3 DPM

To model DPM, we consider a circularly-polarised light beam impinging on the object at the sample plane at normal incidence, and compute the resulting electric field \mathbf{E} at the image plane.

Then, we multiply \mathbf{E} by the transmittance of the 1D grating rotated by 45° around the optical axis (Oz). The pitch of the grating is such that it corresponds to 3 dexels (pixels of the detector). The resulting field is then Fourier-transformed and multiplied by the DPM mask passing the zero order and one 1st order. We shall call D_0 the diameter of the circular crop of the zero order, and D_1 the diameter of the circular crop of 1st order. We considered that the 4- f system was composed of two lenses of focal lengths 10 cm. Finally, the cropped field is back-Fourier-transformed to get the interferogram recorded by the camera. This interferogram is processed using a DPM algorithm to retrieve the phase image φ , which is exactly the same as the DHM algorithm.

3.4 DPC

To model DPC and its 4 tilted illuminations, we reproduced numerically what is usually done experimentally: using an array of point-like sources of light (like a LED array). We chose a circular distribution of sources, with a square unit cell, and with 16 sources along a diameter, leading to 192 sources in total (see the LED array geometry in Fig. S1 in Suppl. Info.). The size of the pattern was adjusted so that it produces a numerical aperture of 0.4 in illumination. We ran a series of 192 numerical simulations, corresponding to all these incident plane waves, all circularly polarized. The single, true phase map φ_{th} is assumed to be

the phase map for normal incident illumination at zero NA. For each numerical simulation j , the intensity map I_j at the camera plane is calculated. Then, these intensity maps are grouped, depending on which side they belong to (top, right, left or bottom, see Fig. S1 in Suppl. Info.), and summed to get the 4 DPC intensity images I_{top} , I_{right} , I_{left} and I_{bottom} , from which the 2 contrast images I_1^{DPC} and I_2^{DPC} are calculated, using Eqs. (10). The intensity and phase PSFs are calculated using the expressions given in Suppl. Info. Then, the phase map is calculated using Eq. (16).

3.5 PSI

To model PSI, we consider a linearly- x -polarised light beam impinging on the object at the sample plane at normal incidence, and compute the resulting electric field \mathbf{E} at the image plane using IF-DDA.

Then, at the image plane, we add the reference beam \mathbf{E}_{ref} , as a linearly x -polarised plane wave at normal incidence endowed with a given, uniform phase shift ϕ : $\mathbf{E}_{\text{ref}} = E_{\text{ref}} e^{i\phi} \mathbf{u}_x$. The intensity recorded by the camera is then simply calculated as $I = |\mathbf{E} + \mathbf{E}_{\text{ref}}|^2$. 4 images are generated, corresponding to 4 different phase shifts ϕ of 0, $\pi/2$, π and $3\pi/2$. These 4 images are then used to compute the phase image φ using Eq. (19).

3.6 FPM

To model FPM, we consider a linearly- x -polarised light beam impinging on the object at the sample plane at normal incidence, and compute the resulting electric field \mathbf{E} at the image plane using IF-DDA. Then, the field is Fourier-transformed and a phase ϕ is applied at the center of the Fourier space, over a circular area. The diameter D_0 of this circular area captures light over an area corresponding to a numerical $\text{NA}_0 = D_0 M / f$ in the object space, where f is the focal length of the tube lens. We then inverse-Fourier-transform the field to get the intensity image recorded by the camera. 4 images are generated, corresponding to 4 different phase shifts ϕ of 0, $\pi/2$, π and $3\pi/2$. These 4 images are then used to compute the phase φ_s of the scattered field using Eq. (19), which is then used to compute the phase image φ of the total field using Eq. (22).

To model a non-zero illumination numerical aperture ($\text{NA}_{\text{ill}} = 0.02$), we consider an ensemble of 13 plane waves corresponding to 13 point sources regularly spaced in the Fourier plane of the illumination (*i.e.*, at the aperture diaphragm location of the Köhler illumination);

3.7 SLIM

To model the annular illumination in SLIM, we run a series of 12 numerical simulations, corresponding to various incident plane waves, all circularly polarized, regularly distributed along a ring around the optical axis (Oz) at an NA of 0.25. For each of the 12 simulations, the true phase map is calculated as the phase map referenced by the phase map of the incident field E_0 at the sample plane. The single, true phase map φ_{th} is assumed to be the average of the 12 phase maps. For each numerical simulation, the \mathbf{E} field is computed, Fourier-transformed, and a phase mask is applied. It consists of an annulus mask, of phase ϕ and transmittance $\tau = 50\%$ (the common transmittance of the phase ring of a phase contrast objective). The radius of the annulus matches the NA of the ring illumination (0.25), and its width is set to a NA of 0.02. The field is then inverse-Fourier-transformed to get the intensity at the camera plane. The intensities of all the 12 illuminations are summed (incoherent summation) to get the image recorded by the camera. 4 of such images are generated corresponding to the 4 values of ϕ : 0, $\pi/2$, π and $3\pi/2$. These 4 images are then used to compute the phase φ_s of the scattered field using Eq. (19) and the β map using Eq. (23), which are then used to compute the phase image φ of the total field using Eq. (22). Note that for SLIM, Eq. (23) must be corrected to take into account the transmittance τ of the phase ring of the objective: $\beta = \sqrt{\tau} |E_s / E_0|$.

3.8 TIE

To model TIE, we simulated three intensity images, I_d , I_0 , I_u of the sample at 3 different focus values of $-\Delta z$, 0 and Δz . Then, the three images were used to process the modelled intensity and wavefront images using the algorithm depicted in Sect. 2.5.

3.9 Noise simulation

We also studied the presence of noise in OPD images. Generally, in QPM, the origin of noise is the shot noise, rather than the reading or thermal noise, because the camera sensor is usually well exposed. Shot noise comes from the discrete nature of light energy (photons) that produces a standard deviation in each dixel equal to \sqrt{N} , where N is the number of photons collected by the dixel. Consequently, the larger the full-well-capacity of the camera, the better the signal-to-noise ratio [53, 55, 56]. For the simulations intended to study the effect of shot noise, we generated noise of the raw camera images using the `poissrnd` function of Matlab, considering a full-well-capacity of the camera of 25,000.

The only source of noise simulated in this article is the shot-noise, inherently present for all techniques. We are aware that other sources of noise can be dominant, especially the coherent noise for techniques requiring laser illumination. We did not simulate this type of noise, but discuss it further on.

To quantitatively compare the noise level of all the QPM techniques for a given object, the object has to be imaged with the same microscope settings (magnification, numerical aperture), and in the same conditions of illumination (at least the wavelength), which is the easy part. The more subtle aspect involves determining the quantity of light collected by the systems. This parameter is crucial as it directly influences the amplitude of noise in the images. It is more subtle because one can imagine different reference conditions, all equally justifiable, namely:

- (i) Camera full-well-capacity filled in any acquired image, no matter how many images the QPM needs to acquire, 1, 3 or 4 (which corresponds to what is done experimentally, most of the time).
- (ii) Equal number of photons detected by the camera, and the illumination intensity is adjusted accordingly for each QPM (to discard the differences in optical transmissions of the QPMs).
- (iii) Equal number of photons impinging on the sample (makes sense when the limitation is cell phototoxicity for instance)

These three conventions are not equivalent. Convention (i) is not equivalent to (ii) because phase

shifting techniques and TIE require the acquisition of several images (resp. 4 and 3), not just one. Then, (ii) is not equivalent to (iii) because QPMs have different transmissions (see Fig. 3). By convention, in Fig. 7, we chose Convention (ii), because Convention (i) would favor phase-shifting techniques that acquire 4 images instead of one, *i.e.*, 4 times more photons leading to a factor of 2 of noise reduction; and not Convention (iii) because phototoxicity is usually not an issue in QPM.

4 Results

This part describes the results of the simulations related to the 8 QPM techniques (CGM, DHM, DPM, DPC, PSI, FPM, SLIM and TIE), imaging 4 different objects, namely a gold nanoparticle, a

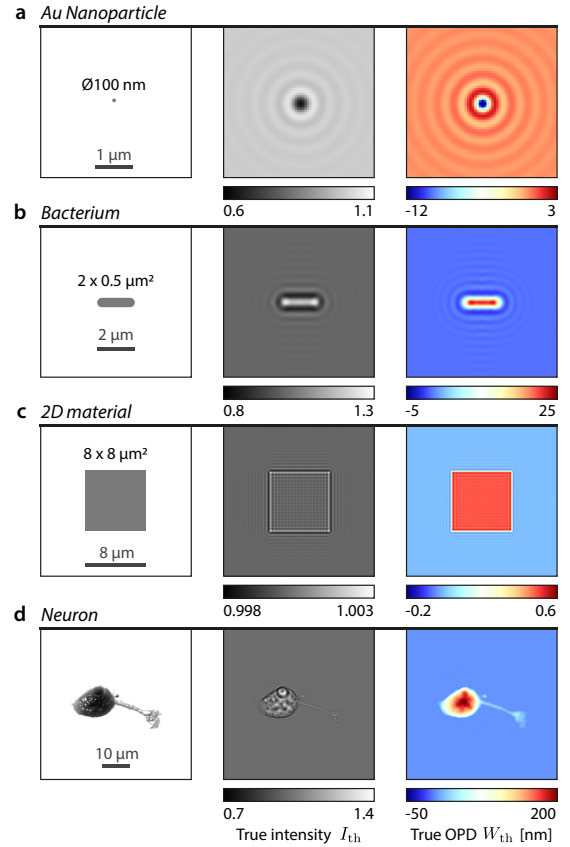


Fig. 5 The 4 objects investigated in this study. (a) The first column defines their geometry, the second displays the theoretical intensity images and the third column displays the theoretical OPD (or wavefront) images.

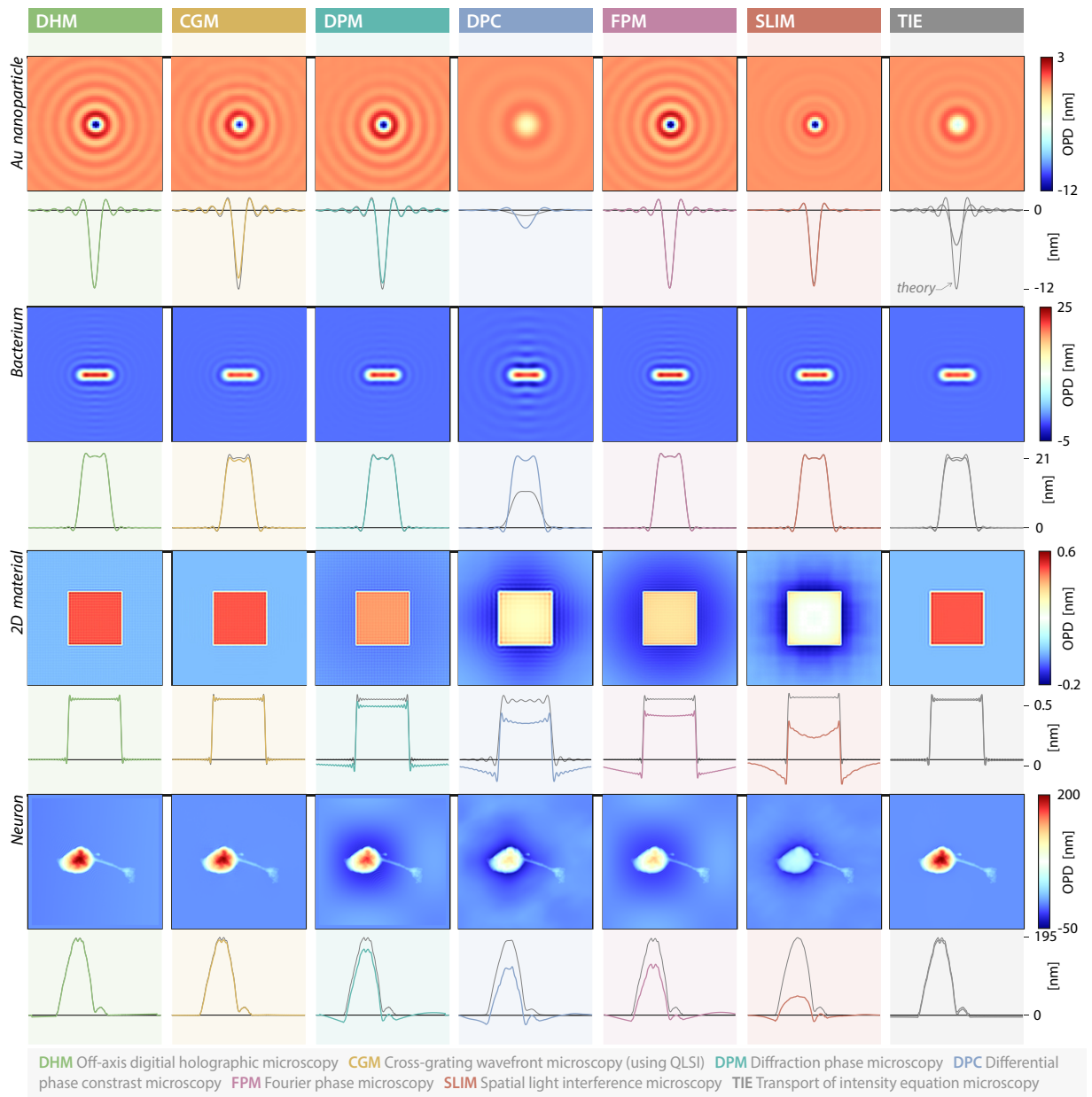


Fig. 6 Investigation of QPM trueness. 28 numerical simulations of OPD images of 4 different objects, acquired using 7 different wavefront and phase microscopy techniques, on the same microscope. Each column corresponds to a microscopy technique. Each row corresponds to an object. For each image, a horizontal crosscut passing through the center of the image is displayed below. The grey lines in the background indicate the theoretical profiles. The experimental setting parameters are: $d = 0.6$ mm for CGM, $D_0 = 20$ μm for DPM, $\epsilon = 10^{-3}$ for DPC, $\text{NA}_0 = 0.02$ for FPM, $\Delta z = 500$ nm for TIE. PSI results are presented in Suppl. Info.

bacterium, a 2D material, and a neuron (Fig. 5). These objects have been chosen because they are commonly studied systems, and because they cover very different object dimensions. The gold nanoparticle (Fig. 5(a)) is spherical, 100 nm in diameter, and immersed in a uniform medium of

refractive index 1.5, to match the experimental conditions of Ref. [51]. The bacterium (Fig. 5(b)) is 2 μm long, 0.5 μm in diameter, lying on glass and immersed in water. It is endowed with a uniform refractive index of 1.38. The 2D material (Fig. 5(c)) is 8×8 μm^2 in size, lying on glass,

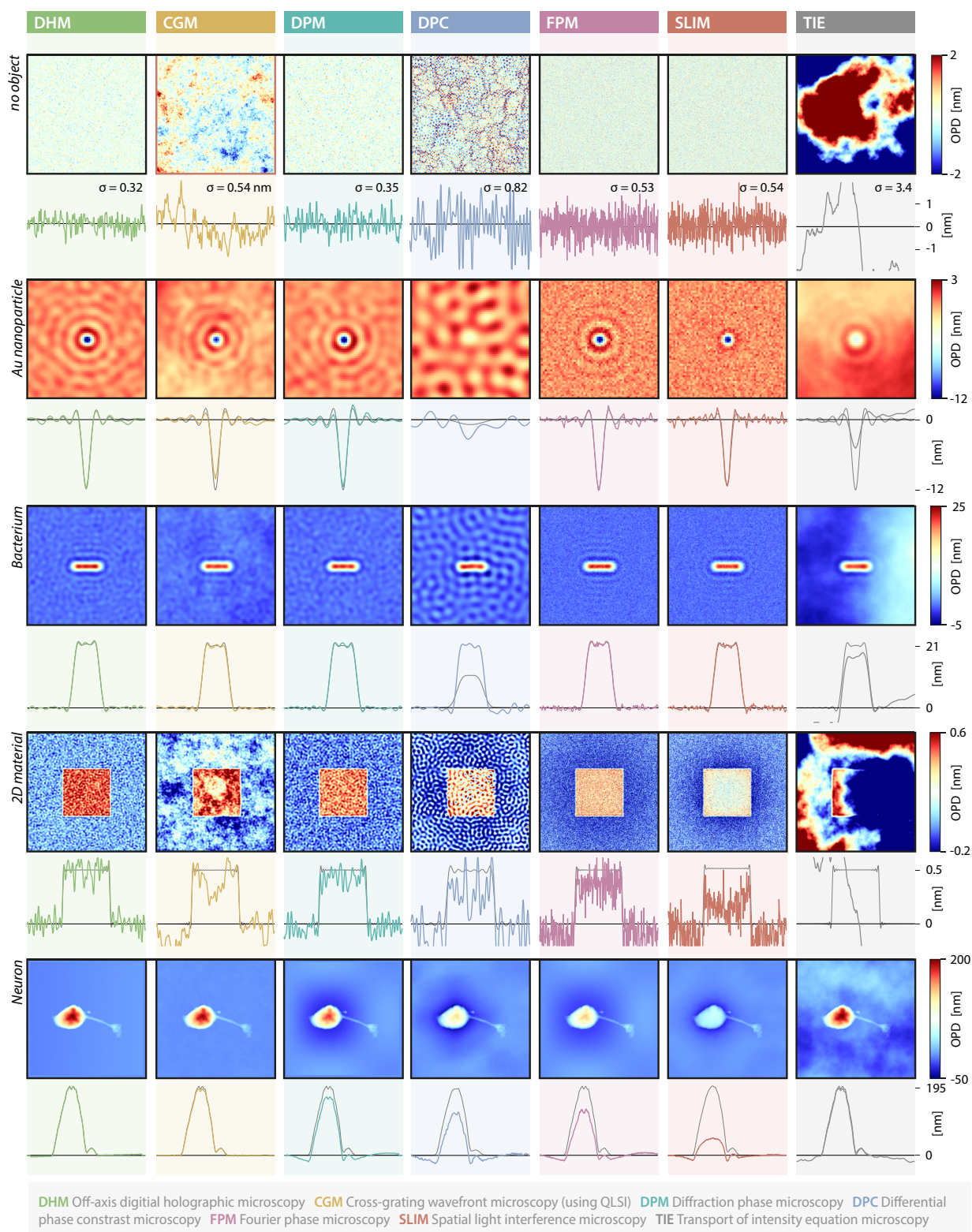


Fig. 7 Investigation of QPM noise amplitudes. 28 numerical simulations of OPD images of 4 different objects, acquired using 7 different wavefront and phase microscopy techniques, on the same microscope. Shot noise has been numerically added to each camera image. Each column corresponds to a microscopy technique. Each row corresponds to an object. For each image, horizontal crosscuts passing through the center of the image are displayed below. The grey lines in the background indicate the theoretical profiles. In the first Row, σ is the standard deviation on the images, in nm. PSI results are presented in Suppl. Info.

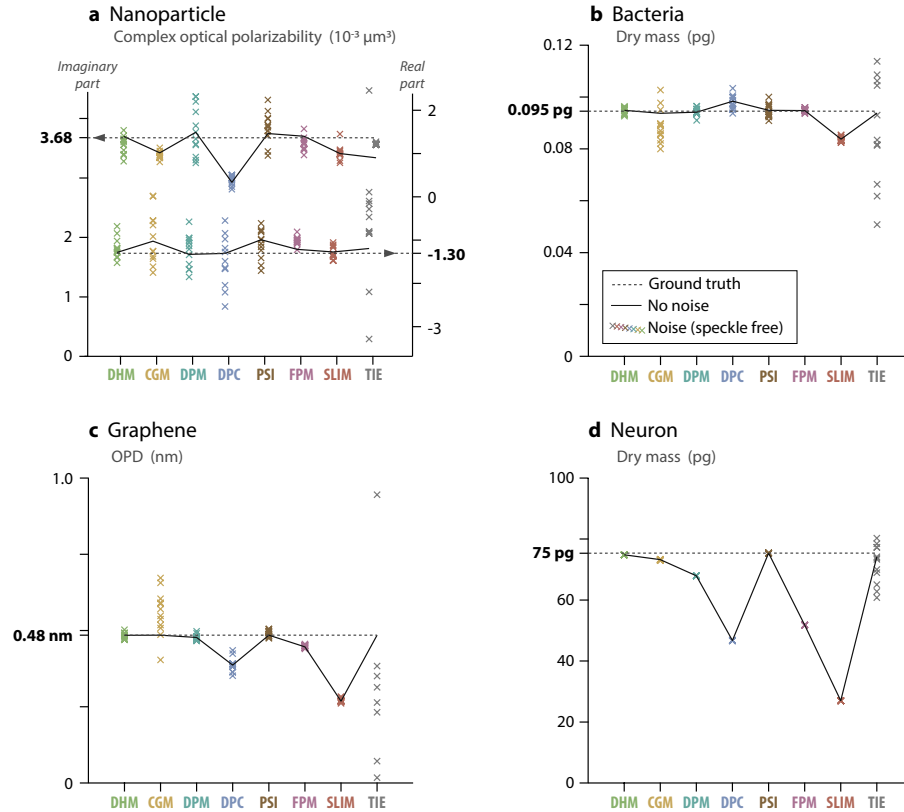


Fig. 8 Biophysical quantities extracted from the simulations of Figs. 6 and 7. (a) Plot of the complex optical polarisabilities of the 100-nm gold NP, measured with each technique. (b) Plot of the dry mass values of the bacteria. (c) Plot of the OPD at the 2D material. (d) Plot of the dry mass values of the neuron. Each graph represents ground truth as dashed lines, while solid lines connect values derived from noise-free images. Data points obtained from sets of 12 noisy (ideal, speckle-free) images are denoted by crosses.

immersed in water, and designed to create an OPD of 0.5 nm, similar to the one of graphene [57]. The 3D model of the neuron (Fig. 5(d)) was created from an experimental image taken from Ref. [57]. It was endowed with a uniform refractive index of 1.38 and the thickness of the cell was set to yield an OPD that was consistent with the experimental measurement. Considering a uniform refractive index within the cell is a strong approximation, but it is sufficient within the scope of this study to evidence the limitations of QPMs for such large objects. For the nanoparticle, bacterium and 2D material, the parameters of the microscope were $\lambda = 532$ nm, $100\times$ magnification, 1.3 NA. For the neuron, they were $\lambda = 600$ nm, $60\times$ magnification, 1.3 NA.

The aim here is to investigate the accuracy of all the QPMs. The accuracy is normally defined as the association of trueness and precision. Trueness

refers to any systematic deviation of the modelled images from the true images, *i.e.*, bias or artefacts, while precision refers to inaccuracy measurements stemming from the noise on the images.

Figure 6 gathers numerical simulations of OPD images of the 4 objects imaged with 7 microscopy techniques, compared with the true OPD images (gray lines labelled 'theory'). Results on PSI are not included in the figures, for space reasons, but they are presented in Suppl. Info, Figure S2. In all these simulations, no shot noise was added to the raw camera images, in order to focus on the presence of possible artefacts.

Figure 7 plots similar data, where shot noise has been added to the raw camera image. This figure is rather aimed to study measurement precision, in terms of signal-to-noise ratio. The 5 investigated systems are (i) a blank area, to better quantify the noise level, (ii) a 100-nm gold nanoparticle, (iii) a bacterium, (iv) a 2D material,

and (v) a neuron. Note that for the 2D material, which features an OPD of only 0.5 nm, 25 images have been averaged for each technique to yield a more reasonable signal-to-noise ratio.

The results presented in Figs. 6 and 7 highlight various levels of noise and deviations from ground truth among the different techniques. In order to quantify the degrees of accuracy of all the QPMs revealed by these simulations, we measured biophysical quantities from all these images. Specifically, we determined the dry mass values of the bacterium and the neuron, the complex optical polarisability of the NP and the average OPD of the 2D material. The dry mass values were evaluated by a pixel summation after tight segmentation of the cells, and the optical polarisability of the NP was determined according to the expression given in [51]. These values are plotted in Fig. 8.

Measurements on the nanoparticle feature the largest lack of precision, being the smallest object (Fig. 8(a)). Even, on the noise-free images, the measurements vary from one technique to another, not really because of artefacts, rather because of the presence of diffraction rings making the segmentation more difficult. The nanoparticle does not feature significant artefacts, for any technique, as observed in Fig. 6. Similarly, measurements on bacteria are not affected by artifacts, regardless of the QPM used (Fig. 8(b)). SLIM just features a weak underestimation. Measurements are mostly inaccurate with large objects, such as graphene (Fig. 8(c)) and eukaryotic cells (Fig. 8(d)); and with DPC, FPM and SLIM.

The presence of noise observed in Fig. 7 makes the biophysical measurements more dispersed around the true value. To quantify this dispersion, we conducted a series of 12 identical simulations, in each QPM/object case, including random shot noise. The 12 measurements are also plotted in Fig. 8, so that this figure gives a general overview of the accuracy of all the techniques, in terms of trueness and precision, as a function of the imaged object. A larger noise affect CGM and TIE images in most cases, in particular for bacteria and graphene.

The following sections aim to explain the origins of all the QPM inaccuracies observed in Fig. 8. We shall discuss the degrees of trueness (artefacts) and precision (signal-to-noise ratio) of

each of the microscopy techniques addressed in this study, one by one.

4.1 CGM accuracy: effect of the grating-camera distance

All in all, the cross-cuts of the OPD images of CGM shown in Fig. 6 are in very good agreement with the theoretical profiles. Nevertheless, one can distinguish a slight discrepancy for the nanoparticle. The slightly reduced peak amplitude observed on the CGM image comes from the grating-camera distance (set at 0.6 mm in all the simulations presented in this Fig. 6). The setting of the grating-camera distance is not critical, in the sense that there is no particular value that makes CGM work. The grating-camera distance d can be continuously tuned, and the interferogram remains well-defined, without being blurred by a Talbot effect, thanks to the $0 - \pi$ checkerboard pattern [33, 35]. Figure 9(a) shows CGM image simulations of the 100-nm gold nanoparticle for various grating-camera distances. The results show that the grating-camera distance must remain below a critical value to yield accurate OPD profiles. Above this limit, on the order of 1 mm for common QLSI systems in microscopy, the OPD amplitude is reduced until a point where 4-fold symmetry artefacts appear on the image [53].

In CGM, the noise of the OPD images is a Flicker noise, also called a Brown noise. It is not a white noise like in most of the other QPM techniques. A Flicker noise is characterised by a larger amount of low spatial frequencies [53], which makes it different from any other QPM technique. More precisely, the power spectral density of the noise in CGM scales as $1/f^2$, where f represents the spatial frequencies of the image. This noise appears as the main drawback of CGM. Fortunately, it is weak, and can be removed by summing images (unlike a speckle noise). However, a Flicker noise is more difficult to remove using postprocessing than a white noise.

As observed in Fig. 9(b), placing the grating further leads to a reduction of the noise amplitude on the OPD images. Moving the grating from 0.2 to 1.4 mm leads to a noise level varying from 1.7 to 0.30 nm. This observation is in agreement with the expression of the standard deviation σ of the

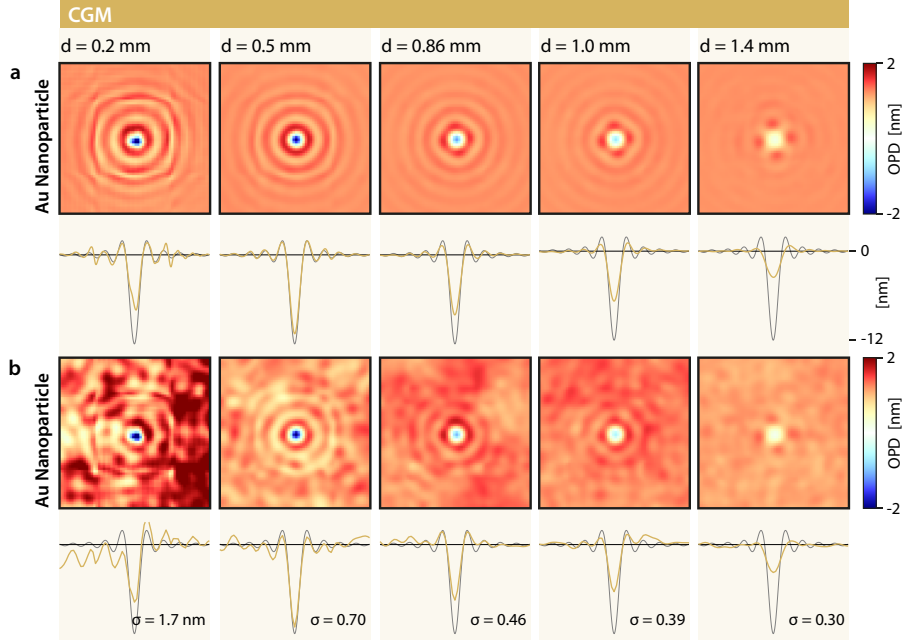


Fig. 9 Influence of the grating-camera distance in cross-grating microscopy (CGM) on trueness and precision. IF-DDA simulations of OPD images acquired with CGM, without (a) and with (b) noise. A cross-cut of the noisy images is displayed in the third row. Each row corresponds to a different grating-camera distance, namely 0.2, 0.5, 0.86 and 1.2 mm. 0.86 mm corresponds to the common distance in CGM, measured on a commercial system.

noise amplitude derived in Ref. [53]:

$$\sigma = \frac{1}{8\sqrt{2}} \frac{p\Gamma}{d} \sqrt{\left(\frac{\log(N_x N_y)}{w N_{\text{im}}} \right)}, \quad (36)$$

where w is the full-well-capacity of the camera, N_{im} the number of averaged images, Γ the cross-grating pitch, p the dixel size, $N_x N_y$ the number of pixels of the image, and d the grating-camera distance. The noise amplitude scales as the inverse of d . Importantly, this $1/f^2$ non-uniformity in the spectral domain makes the noise amplitude dependent on the image size $N_x \times N_y$. The bigger the image, the larger the calculated noise amplitude. This special feature is not really a problem in CGM, because, normally, the larger the object, the thicker it is, like with living cells. However, in the case of thin and extended objects, such a low-frequency noise can be problematic. This is why the OPD values are particularly dispersed in Fig. 8(c) related to graphene, in the case of CGM, while they are not in the case of a neuron (Fig. 8(d)).

However, the grating cannot be placed arbitrarily far, as artefacts begin to appear, as previously explained. In CGM, there exists therefore a trade-off between trueness and precision when adjusting the grating position.

CGM is inherently achromatic because it is sensitive to the shape of a wavefront, rather than the phase of light. It is commonly employed with incoherent, broad-band illumination from an LED or a bulb, sometimes in conjunction with a band-pass filter. CGM could be used with a laser illumination, but it is usually avoided because it creates the same speckle noise and fringes as the ones observed in DHM and PSI. There are two consequences of this. First, there is no other noise origin than the shot noise. In particular, there is no speckle noise. The noise level that is observed experimentally is exactly what is observed numerically in this work [53]. Second, there is always a non-zero illumination NA. Opening the illumination NA is likely to create artefacts in QPM, like with DPM and FPM as explained further on (Figs. 11 and 13). However, it is not the case in CGM, unless large NA are used (typically above 0.6), as explained in Refs. [14, 53]. When such artefacts related to the illumination NA occur, an image

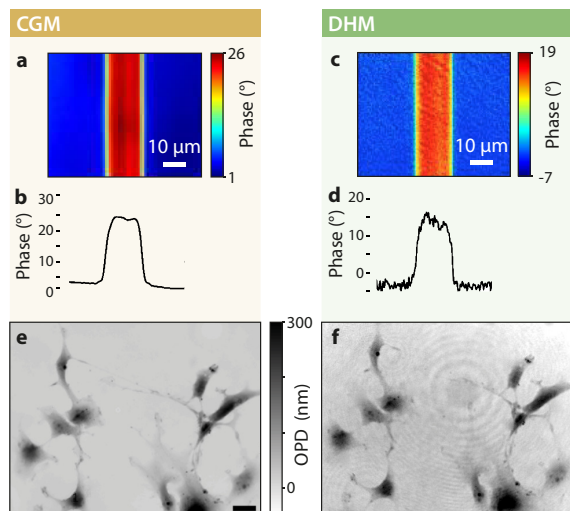


Fig. 10 Comparison between DHM and CGM. (a) Phase image of a waveguide acquired using CGM, along with (b) an horizontal crosscut. (c) Phase image of a waveguide acquired using DHM, along with (d) a horizontal crosscut. Reprinted with permission from ref [27]. Copyright 2018 Optical Society of America. (e) OPD image of fixed COS-7 cells obtained using CGM (40×, 1.3 NA) and (f) OPD image of the same cells obtained using DHM (20×, 0.7 NA). The color bar and scale bar are common to both figures. Reprinted with permission from Ref. [28]. Copyright 2019 Optical Society of America.

post-processing can be applied to correct for the artefacts, as explained in [14].

4.2 Accuracy of DHM and PSI

DHM and PSI have similar experimental implementations (Figs. 2b,f). They represent respectively the simplest implementations of off-axis and phase-shifting methods, and exhibit perfect, artefact-free phase images for any system (Fig. 6, 2nd and 4th columns). There are no inherent artefacts associated with these methods.

These techniques also offer the possibility to adjust the relative intensities of the two arms, as a means to improve the contrast of the interferogram, a benefit that DPM does not possess for instance.

In the simulation of Fig. 7, DHM exhibits a very acceptable noise level compared with all the other QPM techniques. However, our simulations using IF-DDA aim to quantify the inherent inaccuracies and noise levels for each system, free from imperfections. In practice, when using a laser illumination to make an image on a camera, the image

is naturally degraded by a speckle noise and by fringes. We cannot render this type of noise in our simulations, because we model perfect illuminations and microscopes. Our numerical simulations for DHM and PSI are thus better than reality, in terms of signal-to-noise ratio. However, our simulations are not disconnected from reality because methods exist to substantially reduce the amplitude of speckle noise in DHM [58] and PSI [59], which is a very active research line in the QPM community.

Unlike shot-noise, or Flicker noise in CGM, a speckle noise cannot be eliminated by averaging images (unless the illumination varies over time). This noise is random in space, not in time, which is why it is particularly problematic.

In 2018, Bellanger *et al.* presented a comparative study of CGM and DHM [27]. One of the objectives of this article was to experimentally compare the noise levels of these two techniques. We reproduce in Figs. 10(a)–(d) their results on the measurements of the phase profile of a waveguide. The effect of the coherent noise is visible on the DHM images. As a result, the noise level is higher for DHM compared with CGM. In Figs. 10(e) and 10(f), taken from Ref. [28], also comparing CGM and DHM, the presence of fringes in DHM is evidenced.

4.3 DPM accuracy: influence of the zero-order pinhole

DPM operates on the same principle as DHM. It is an off-axis technique that generates phase-related information through interference with a reference plane wave. However, the implementation is distinctly different, as it is a common-path method. In DHM, the reference beam follows a separate path (Fig. 2(c)). In DPM, the reference beam is created from a replica of the image itself, in which the lowest spatial frequency is filtered by a pinhole in the Fourier space, as a means to get a quasi plane wave (Fig. 2(d)). The diameter D_0 of the pinhole in the DPM mask is crucial. It has to be as small as possible, ideally a point, to efficiently filter all the non-zero spatial frequencies of the corresponding light profile at the image plane, to obtain a plane wave acting as the reference beam, like in DHM. When the pinhole is too large, some non-zero, low spatial frequencies are transmitted, and all these low frequencies are subtracted to the

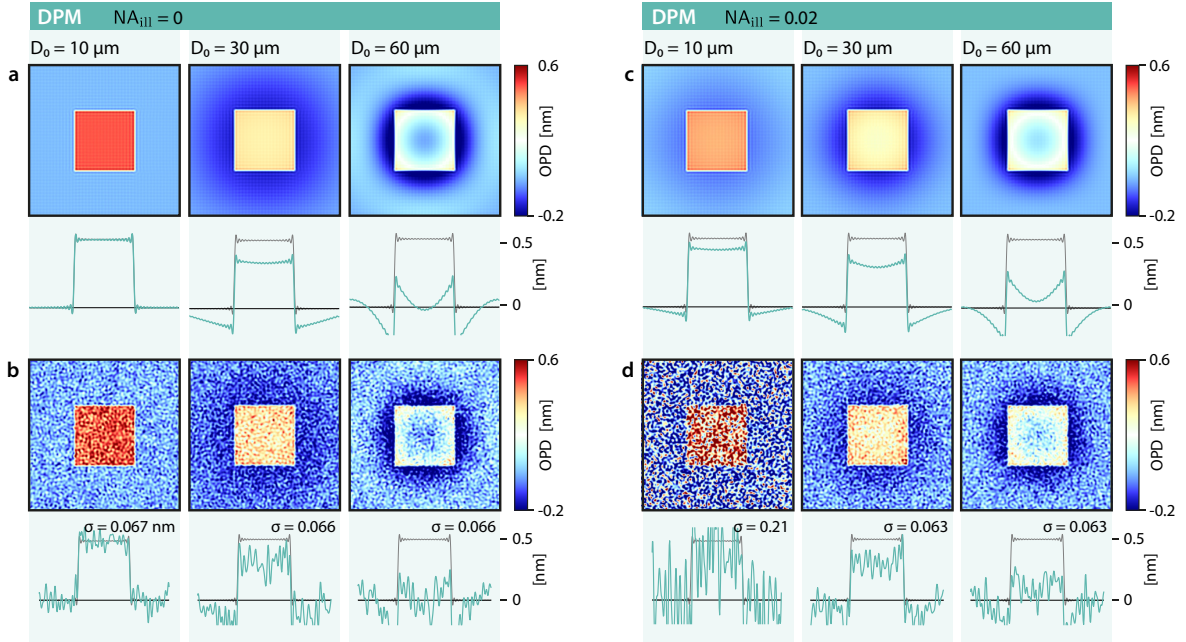


Fig. 11 Influence of the size of the 0-order pinhole in diffraction phase microscopy (DPM) on trueness and precision. IF-DDA simulations of OPD images acquired with DPM, without (a,c) and with (b,d) noise, along with crosscuts. While (a,b) correspond to a plane wave illumination of the sample, (c,d) corresponds to an illumination with a NA of 0.02. Each row corresponds to a different pinhole size, namely 10, 30 and 60 μm .

final image, leading to an area of inverted contrast around the object of interest. This effect is called the *halo effect* [46, 60, 61]. The halo effect in DPM can be observed in the literature (see an example in Fig. 1(d)). Such an artefact is also observed in DPC, FPM and SLIM (Fig. 1(e)) but the origin is different, as explained in the next sections. Referring to it as a *halo* underestimates the issue because it implies that the problem only occurs outside the object of interest. However, each time a halo effect appears, it implies a reduction of the OPD within the object as well, sometimes called the *shade-off effect* [60], affecting the precision of any quantitative measurements, for instance of the dry mass of the cell. In Figs. 1(e) and 1(f), the more problematic shade-off effect is even more obvious than the halo effect.

Common DPM pinhole sizes reported in the literature are 10 μm [62, 63], sometimes 15 μm [64]. Some articles even report pinhole sizes of 100 μm , 150 μm [65], or even 200 μm in [13, 66]. In Fig. 11(a), we show numerical results of a 2D material imaged by DPM with various pinhole sizes, ranging from 10 μm to 60 μm , where the halo and shade-off effects are observed above $D_0 = 10 \mu\text{m}$. This effect of the pinhole size in

DPM explains why some articles report abnormal OPD-flat eukaryotic cells and some others not: the introductory Fig. 1(c) looks consistent, while Fig. 1(d) looks problematic, although both of them were acquired using DPM.

Figure 11(b) shows the same simulations with shot noise added to the interferogram. Interestingly, the size of the pinhole does not affect the amplitude of the noise, at least for this system consisting of a thin object.

The rule for the pinhole size in DPM appears to be 'the smaller, the better' and while generally sound, it does have limitations in at least two scenarios, which we elaborate on below: the observation of thick/large objects and the use of incoherent (white light) illumination.

When working with thick, scattering objects, or objects covering a large part of the field of view, *i.e.*, with an object scattering a large amount of the incoming light out from the direction of the optical axis, the zero-order spot in the Fourier plane becomes broad, and possibly larger than the pinhole size. In that case, if small enough, the pinhole effectively produces a plane wave, but of weak intensity compared with the first order. The two

interfering light beams have thus different intensities, leading to poor fringe contrast and thus a higher noise level.

Some studies reported the use of DPM with incoherent light sources, an approach called white-light DPM (wDPM) [66]. DPM can be much more easily used with an incoherent illumination, compared with DHM, because it is a common-path technique. In that case, the source is not a laser, but rather an LED or a bulb, and the numerical aperture of the illumination cannot be zero. As a consequence, the spot size in the Fourier plane (where the pinhole lies) is necessarily broader than with a laser. Regarding the pinhole size, there are two options: (i) either its size is big enough to capture this bigger 0-order spot. In that case, the contrast of the fringes will be optimized because the 0 and 1st orders have comparable intensities. However, there is a risk to capture non-zero, low spatial frequencies that could create halo/shaded-off artefacts, as observed in Fig. 11(c) even at $D_0 = 10\text{ }\mu\text{m}$; (ii) or the size of the mask is as small as possible, to avoid halo/shade-off artefacts. But in that case, the intensity of the 0-order is strongly reduced compared with the 1st order, reducing the contrast of the fringes and increasing the noise level on the images, as observed in Fig. 11(d). In white-light DPM, there is a trade-off between accuracy and noise, exactly like in CGM with the grating-camera distance, but for a totally different reason.

Some procedures have been developed to correct for the halo effect [67], but they are questionable, because artificially adding some low frequencies where the imaged objects are lying, and they are not always effective: For instance, in the article where Fig. 1(d) was taken, the halo effect is said to be corrected, but the soma of the cell in the OPD image still appears empty. In 2021, deep learning was proposed as a method for correcting for the halo effect in DPM [68].

4.4 DPC accuracy

The DPC simulations presented in Fig. 6 show significant deviation from theory, regardless of the imaged object. The theory profiles are naturally different from all the other techniques because DPC uses a small NA objective (0.4 compared with 1.3 for the other techniques). For small

objects, the simulated profiles look super-resolved, while for large objects, there is a halo/shade-off effect. The two next subsections explain these observations.

4.4.1 DPC accuracy: influence of the numerical apertures

The only experimental degree of freedom in DPC is the NA of the 4-quadrant illumination. It has been elucidated and experimentally demonstrated in Ref. [23] that this illumination NA must align with the NA of the objective lens. Our IF-DDA simulations confirm this requirement. In Fig. 12, we show the image of the neuron with $(N_{\text{ill}}, N_{\text{obj}}) = (0.4, 0.4)$ and $(N_{\text{ill}}, N_{\text{obj}}) = (0.4, 0.8)$. In the latter case, the object totally disappears. This restriction necessitates the use of a low-NA objective, resulting in reduced spatial resolution in DPC compared to all the other QPM techniques. However, it is important to note that the effective NA in DPC equals $N_{\text{obj}} + N_{\text{ill}}$, *i.e.*, 0.8 here. This benefit enhances the initial spatial resolution by a factor of 2, but it remains low compared with the case of oil-immersion objectives. It is why the simulated DPC images look super-resolved in Fig. 6, compared with theory.

4.4.2 DPC accuracy: influence of Tikhonov regularization parameter α

The other important degree of freedom in DPC is not experimental, but numerical. The Tikhonov regularization parameter ϵ is an artificial offset in the denominator of Eq. (16). It avoids division by small values to prevent a high noise level. The side effect of this artificial offset is a damping of the retrieved φ . Reference [23] mentions that a good compromise is $\epsilon = 10^{-3}$. It is the value we used in all the simulations presented in Figs. 6 and 7. In Fig. 12, we compare images of neurons obtained with $\alpha = 10^{-3}$ and $\epsilon = 10^{-5}$. While the halo/shade-off effect is important for $\epsilon = 10^{-3}$, it is well reduced for $\epsilon = 10^{-5}$. This latter value is therefore more recommended, especially if quantitative dry mass measurements is the aim of the study. It, however, comes along a high noise level, as observed in Figs. 12d–f, which can be discarded by average multiples images, or using a camera with a large full-well-capacity.

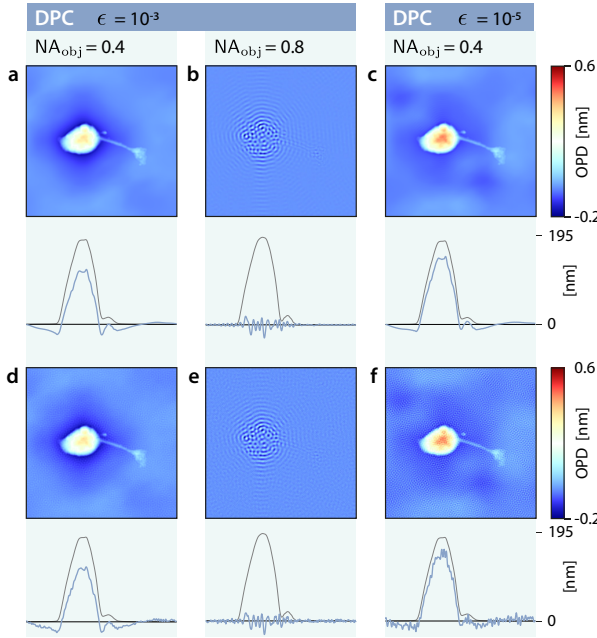


Fig. 12 Influence of the objective NA and the Tikhonov parameter ϵ in differential phase contrast microscopy (DPC) on trueness and precision. (a) Noise-free IF-DDA simulation of the OPD image of a neuron acquired with DPC, with an objective NA of 0.4, and $\epsilon = 10^{-3}$. (b) Same as (a), with an objective NA of 0.8. (c) Same as (c) with $\epsilon = 10^{-5}$. (d-f) Same as (a-c), with noise.

4.5 FPM accuracy: influence of the size of the circular phase mask

Although FPM belongs to the other family of phase-shifting techniques, it is experimentally similar to DPM because it plays with the zero-order spot in the Fourier plane. However, in FPM, this spot is the only one in the Fourier space (no 1st order diffraction spots created by a grating), and it is captured by a phase mask, the dimension of which is expressed here in numerical aperture NA_0 . This similarity makes FPM suffer from similar problems as DPM, also leading to a halo/shade-off effect for some specific values of the free parameter, here NA_0 .

In FPM, the phase shifts (of 0 , $\pi/2$, π , and $3\pi/2$) are supposed to be applied to the unscattered field E_0 , ideally only present at $NA = 0$ (point-like spot in the Fourier space). If NA_0 is too large, *i.e.*, if the size of the phase mask created by the SLM in the Fourier space is too large, the phase shifts are not only applied to E_0 but also to a part of the scattered field NA_s , the low spatial-frequency part, artificially incorporating it

into E_0 , leading to a halo/shade-off effect. This issue is shown in Fig. 13(a), where such artefacts appear when the mask size is increased. This effect is all the more important for objects with low spatial frequencies, *i.e.*, large objects, as observed for the 2D material or the cell in Fig. 6.

Just like in DPM, one could conclude that making NA_0 as small as possible is the golden rule. However, it is not always recommended. Indeed, unlike with DPM, there is a lower limit to the free parameter NA_0 in FPM. NA_0 should never be smaller than the illumination NA, NA_{ill} . Otherwise, the phase mask is not capturing the whole E_0 field. If NA_0 is too small, such that $NA_0 < NA_{ill}$, then part of the incoming field E_0 is not phase shifted, which creates a halo/shade-off artefact. This problem occurs in particular when using incoherent (called white-light) illumination. FPM was demonstrated using white light, a modality called wFPM [69]. In that case, the zero order is naturally not a point in the Fourier space. This problem is observed in Figure 13c, with NA_{ill} was set to 0.02, which is an extremely small value. For $NA_0 = 0.015$, just below NA_{ill} , the signal is completely lost. This makes a strong difference with DPM, where reducing the crop never yields artefacts, and just increases the noise level. Here, with FPM, artefacts occur systematically when the phase mask is too large, but also when it is too small. And sometimes, especially with wFPM, no phase mask dimension leads to quantitative measurements. In Ref. [69], where wFPM was introduced, we can see that the imaged red blood cells suffer for the shade-off effect, because the central part of the RBCs feature a zero OPD value. RBCs are supposed to exhibit a lower OPD value in the center, but not a zero value. Just like wDPM, wFPM is not recommended when the quantitateness of the measurements is important.

Regarding the noise level, changing the phase mask size has no effect on the noise level, in any case, because it does not modify the light intensity reaching the camera sensor (Figs. 13(b) and 13(d)). This observation is much different from what happens in DPM, where a reduction of the hole size in the Fourier plane decreases the fringe contrast and thus increases the noise level (see Fig. 11).

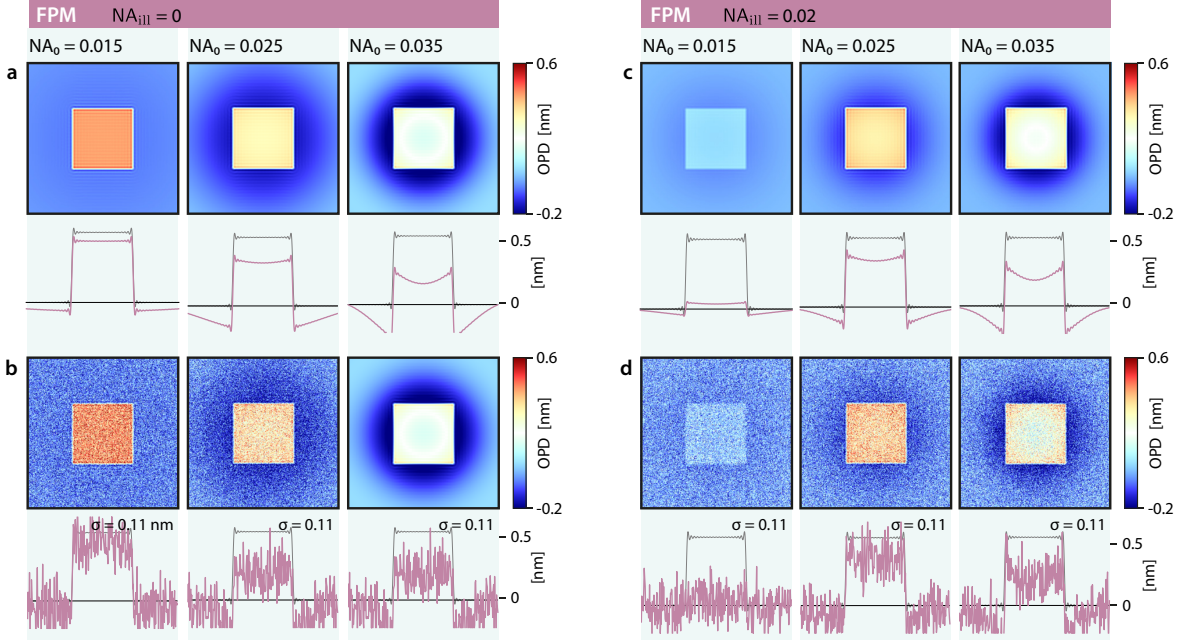


Fig. 13 Influence of the 0-order mask diameter in Fourier phase microscopy (FPM) on trueness. IF-DDA simulations of OPD images acquired with FPM, without (a,c) and with (b,d) noise, along with crosscuts. While (a,b) correspond to a plane wave illumination of the sample, (c,d) corresponds to an illumination with a NA of 0.02. Each row corresponds to a different numerical aperture of the phase mask NA_0 , namely 0.015, 0.025 and 0.035.

4.6 Inherent inaccuracies of SLIM

In general, in our simulations, what is assumed to be the theoretical OPD profile (*i.e.*, the ground truth) is the OPD profile under plane wave, normal illumination. The first problem with SLIM is that the illumination is not a plane wave, and not normal. SLIM involves an annular illumination. The question of what the definition of the true OPD should be is thus raised. In the IF-DDA simulations related to SLIM, the annular illumination is composed a 12 tilted plane waves regularly distributed along a circle in the Fourier plane at an NA of 0.25. We considered the theoretical OPD to be the average of the 12 OPD images calculated using IF-DDA, corresponding to 12 titled plane wave illuminations. This average OPD slightly differs from the OPD obtained under normal incidence (see the solid 'theory' grey lines in Fig. 6 for the nanoparticle simulation, compared with the other theoretical profiles on the same row). The numerical simulations show that SLIM tends indeed to measure this average OPD (Fig. 6). However, this quantity can differ from what would be measured using any QPM based on a plane wave illumination.

The second problem with SLIM is the halo/shade-off effect [70]. The origin of the effect is exactly the same as in FPM (see previous section 4.5). SLIM encounters difficulties as soon as objects cover a large part of the field of view, because large objects feature low spatial frequencies that tend to overlap with the phase mask. The problem with SLIM is even more important compared with FPM, because in SLIM, one cannot play with the size of the mask. First, it has an annular shape, and then its dimensions has to match the dimensions of the annular phase mask of the phase-contrast objective lens. And second, this objective's annular phase mask is far from being infinitely thin. While halo artefacts can be avoided in FPM using a laser illumination and small enough a phase mask, SLIM is thus bound to feature important halo effects for large objects. Figure 6 illustrates this problem, where artefacts are visible for large objects such as the 2D material and the cell. Note that we used a width of 0.02NA for the annular mask, which is much better than the specification of phase contrast objectives (rather on the order of 0.1). Nevertheless, artefacts are still observed. It also explains

the artefact observed in the experimental measurement of Fig. 1(e). Unlike FPM, where the size of the 0-order phase mask can be reduced in size, there is no degree of freedom in SLIM, and one has to live with this artefact. SLIM looks more suited to characterise small objects, like bacteria or nanoparticles (see Fig. 6).

Numerical methods have been developed to correct for the halo effect [67, 70]. However, they consist of adding a blurry image to the image, to artificially add some low frequencies and visually improves the rendering of the image. However, the claim that this trick recovers the true OPD image is not obvious, and this method tends to correct only the halo effect and not the shade-off effect.

4.7 Effect of the defocus parameter in TIE

In TIE, three intensity images need to be acquired at various focuses ($-\Delta z$, 0 and Δz) to reconstruct an OPD image [71]. Figure 14(a) displays OPD images generated by TIE on a nanoparticle. In general, the smaller Δz the better. At distances larger than 0.5 μm , the OPD spreads and becomes underestimated. For larger objects, like the neuron in Fig. 14(b), larger defocus parameters can be used. The only issue is a loss of spatial resolution [71], which is evidenced by closely looking at the neurite in Fig. 14(b). Unlike FPM or DPM, there is no creation of artefacts with TIE when increasing the free parameter. It just yields a loss in spatial resolution.

Figure 7 evidences a much higher degree of noise for TIE compared with the other QPMs. The reason is certainly that, unlike all the other QPMs, TIE is not an interferometry technique, in the sense that the phase map does not arise experimentally from an interference mechanism. TIE images simply arise from the subtraction of quasi-identical intensity images, I_u and I_d (Eq. (31)), making the resulting image very sensitive to shot noise from the beginning of the algorithm. Moreover, TIE primarily measures the Laplacian (2nd derivative) of the wavefront (Eq. (24)), while CGM measures the gradient (1st derivative). Thus, two integration steps are required in TIE, which leads to a high amount of low-frequency noise ($\sim 1/f^4$), much more than CGM ($\sim 1/f^2$). As a consequence, this technique is not particularly suited *a priori* for imaging small or

thin objects, such as nanoparticles or 2D materials. However, the technique performs nicely for eukaryotic cells. Figures 14(c) and 14(d) show images of a nanoparticle and a living cell. To faithfully image a nanoparticle, the defocus has to remain below $\pm 0.2 \mu\text{m}$, making the image very noisy and not really exploitable. However, for large and thick objects, such as eukaryotic cells, the defocus can be much larger without creating artefacts in the images. The drawback is rather a loss of spatial resolution on the images. This is a strong difference with other QPMs such as FPM or CGM, where the setting of the parameter comes along with a trade-off between trueness and precision.

5 Other comparison parameters

5.1 Instabilities

A problem that is not represented in our numerical simulations is the instabilities, which are defects that are not inherent to the technique, but coming from experimental imperfections (air flow on the setup, temperature variations, vibrations). Sometimes, they can be the main source of measurement inaccuracies. This is important because imperfection can substantially contribute to the image quality for some techniques, especially in DHM. Because there is a spatially separated arm, differences can happen between the two arms, and because of the sensitivity of interferometry measurements, even weak and unavoidable perturbations such as air flow, temperature variations or vibrations can substantially affect measurements using DHM, and even more using PSI, which is not single shot.

This problem explains the emergence of common-path techniques, which remain interferometric but discard the presence of a reference arm, such as DPM or CGM. These techniques are much less sensitive to external perturbations because the two interfering beams propagate along a common path. In CGM, the interference between the four diffracted beams occur over the caged millimetric distance between the grating and the camera, where there is no air flow. For CGM homemade systems using a relay lens, there may be a flow creating instabilities, but they can be easily discarded by shielding the beam path with tubes.

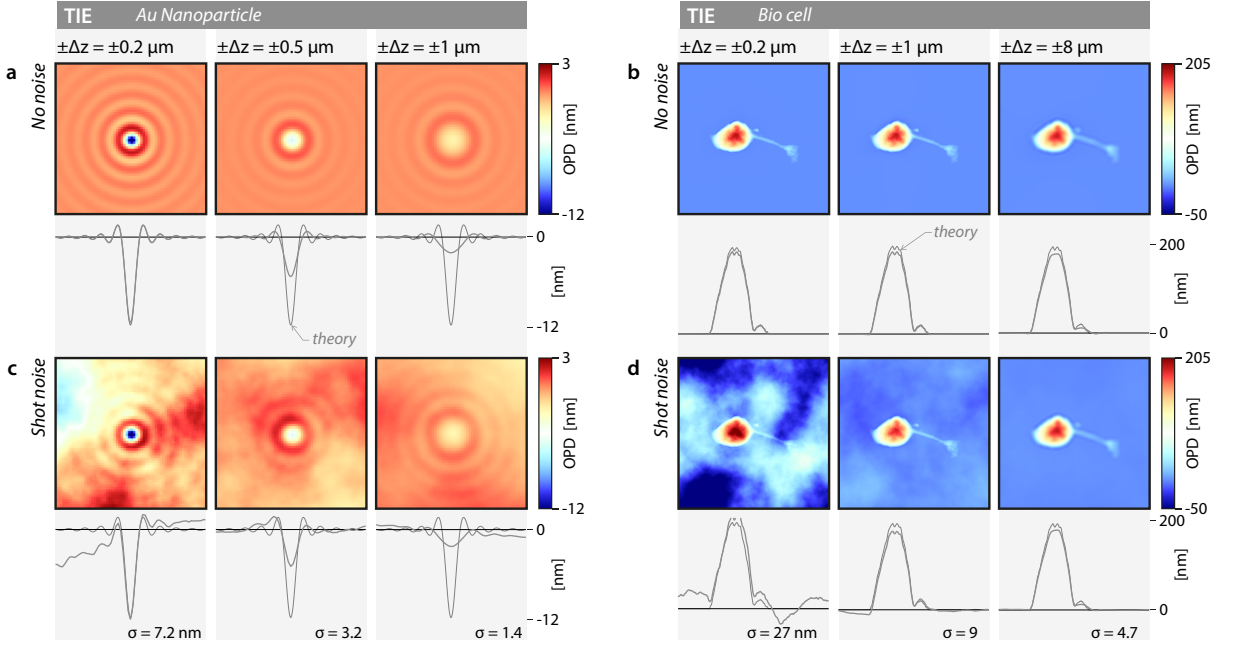


Fig. 14 Influence of the defocus variation on the image reconstruction accuracy in transport-of-intensity equation microscopy (TIE). (a) Noise-free images of a nanoparticle imaged by TIE as a function of the defocus Δz , along with horizontal cross-cuts. (b) Same as (a) for a biological cell. (c,d) Same as (a,b) with shot noise.

For techniques requiring multiple acquisitions (PSI, FPM, SLIM and TIE), the sample movements (including thermomechanical drifts) can be a major source of error. Parallelized acquisition to simultaneously measure the required multiple images has been proposed for TIE to overcome this limitation [72].

5.2 Image noise

We have explained that CGM and TIE feature a high degree of noise level, because they rely on integration steps that enhance low-spatial-frequency noise (Flicker noise). However, this type of noise can be arbitrarily reduced by averaging imaging.

The other source of inaccuracies that cannot be taken into account in numerical simulations is the speckle noise, that occurs as soon as a laser illumination is used. It is the case in DHM, PSI, and in general for any QPM based on the use of two arms.

Unlike shot-noise, or Flicker noise, a speckle noise cannot be eliminated by averaging images. This noise is random in space, not in time, which is why it is particularly problematic.

Some approaches have been developed, both in DHM [58] and PSI [59], to reduce speckle noise, including optical and numerical methods. For instance, a noise reduction can be achieved with different positions of the camera or of the object, by using different longitudinal laser modes, or by using a tunable light source [58]. Also, the use of a partially coherent source is possible in DHM, as long as some caution is used [73]: the separate paths of the object and reference arms have to be carefully matched to obtain contrasted interference. Moreover, conventional DHM, using a tilted mirror like in Fig. 2(c), would fail in producing a contrasted interferogram throughout the full field of view, because the optical path difference cannot be uniform. The trick consists in using a grating instead of a tilted mirror. This second constraint is lifted when using PSI [59], but PSI does not require a tilt.

5.3 Speed

Some QPMs require the acquisition of several images to reconstruct a single OPD image. It is the case of phase-shifting techniques (PSI, FPM, SLIM), which acquire 4 images, DPC which requires at least 4 images as well, and TIE, which

requires 3 images. Note that more than 4 images can be acquired with DPC, to avoid possible 4-fold symmetries on the phase images [23]. Also, more than 3 images in TIE can be acquired to improve the signal-to-noise ratio. And 3 images could be sufficient in phase-shifting techniques in theory, but 4 is highly recommended to gain in signal-to-noise ratio. Multiple acquisitions make the study of dynamical processes more complicated if they are fast. The speed of all the other QPM techniques (CGM, DPM, DHM) just equals the camera frame rate, and are considered fast for this reason.

Note that a reduced speed, due to the acquisition of multiple images, is usually not a strong drawback when investigating physical samples or even cells in culture, where the dynamical processes are usually slow.

5.4 Simplicity/compactness

DHM or PSI require the full modification of a microscope, both in illumination and detection. They do not qualify as compact.

However, CGM just consists of a simple camera, to be implemented in the port of a standard wide-field microscope. It is the most compact technique one can think of, because this benefit does not exist with any other QPMs.

TIE also consists of using a simple microscope the way it is. No additional bulky system is required. It is thus particularly simple and cost effective.

DPC requires the implementation of a LED array in place of the illumination.

DPM, SLIM and FPM systems are more bulky, but they also consist of add-on modules to be adapted on the port of optical microscopes.

5.5 Chromaticity

The ability to vary the illumination wavelength, or the ability to use broadband illumination are valuable assets in QPM, but not all the QPM techniques have these abilities.

As soon as an SLM is used, *i.e.* with FPM or SLIM, a specific wavelength (or tight wavelength range) has to be used, matching the calibration of the SLM. FPM and SLIM are thus not likely to easily conduct wavelength-dependent studies. However, SLIM does not require a laser illumination. DPM and FPM can also use incoherent light

sources, modalities called wDPM [66] and wFPM [69], but at the cost of a reduced accuracy (see Sects. 4.3 and 4.5).

Techniques based on laser illumination, such as DHM or PSI, are also not likely to conduct wavelength dependent studies because wavelength-adjustable lasers in the visible range and much less common and more expensive than monochromators. Monochromators and wavelength-dependent studies can however be straightforwardly conducted using CGM or TIE.

5.6 Absolute/relative measurements

There exist two QPM families, those actually measuring phase, and those rather imaging wavefronts (see first line of the table in Fig. 3). The wavefront imaging techniques are CGM and TIE. Because they firstly image wavefront gradients that are eventually integrated, an additive constant appears, making the measurements not absolute. In other words, the OPD map is obtained to within a constant. Consequently, CGM and TIE are not sensitive to global variations of the phase over the field of view, also called a piston. Indeed, in TIE, a global phase variation does not modify any of the acquired intensity images I_u , I_d and I_0 , precisely because they are intensity images. In CGM, a global phase variation does not modify the spot-array pattern of the interferogram. Albeit a phase imaging technique, DPC also provides relative measurements because it primarily measures phase gradients. Indeed, DPC is not interferometric and any piston does not modify the set of regular intensity images acquired with DPC. However, in DHM for instance, progressively varying the global phase over the field of view results in a progressive fringe shifting in the interferogram. Thus, CGM and TIE (wavefront imaging techniques) provide wavefront profiles to within a constant, while phase imaging techniques are capable of measuring absolute phase variations, in theory.

However, getting the phase/wavefront to within a constant is not a limitation in most applications, especially in cell biology. For instance, dry masses can be still easily measured in CGM considering that the outer boundary of the object in the OPD image is zero [29, 74, 75].

5.7 Polarisation

Some samples can be birefringent, meaning that their refractive index depends on the polarisation of the incident light. It is the case of collagen fibers, or anisotropic nanoparticles for instance. Birefringence characterisation is possible using techniques such as CGM [52, 76] or DHM [77] by rotating the polarisation of the incident illumination, or by implementing a polarizer in detection. However, any QPM based on the use of an SLM (*i.e.* SLIM and FPM) cannot study birefringence because an SLM requires a linearly polarised light beam along a given direction.

5.8 Spatial resolution and image definition

CGM, DHM and DPM belong to the same family of off-axis QPMs. They all rely on the acquisition of an interferogram, characterized by fringes, from which the OPD image can be retrieved from a single image, at the cost of a reduction of the number of pixels of the image, compared to the camera raw image. One usually has an area of 3×3 pixels of the raw image (interferogram) that corresponds to 1 OPD pixel [15, 53]. This reduction of image definition does not necessarily lead to a reduction of the image resolution. If the microscope oversamples the object, then the diffraction limit can still be reached [56, 78, 79].

On the contrary, DPC, PSI, FPM, SLIM, TIE do not gain information by sacrificing some image definition, but by acquiring multiple images. Thus, with these techniques, the processed OPD and intensity images have the same number of pixels as the raw camera image.

DPC is special in the sense that it requires a low-NA objective, typically with a NA value of 0.4. Since the illumination NA has to match the objective NA, the effective NA in DPC is twice as large, *i.e.* 0.8. However, it is still smaller than what the other QPMs can do. The spatial resolution in DPC is thus usually poorer than with other QPMs.

6 Summary

The aim of the article is twofold, (i) present and share a numerical toolbox tailored to modeling

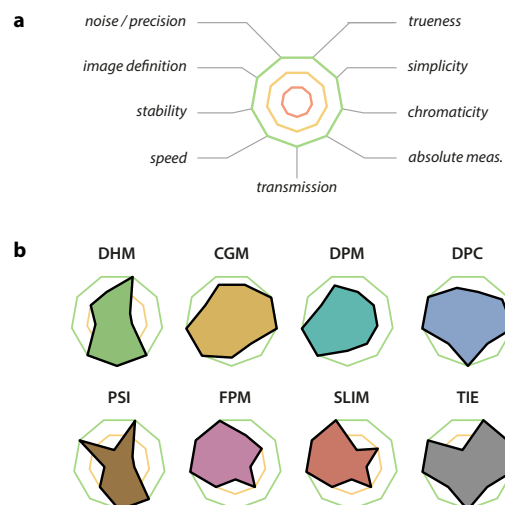


Fig. 15 Comparison of QPM features. (a) Designation of the features of the radar charts. (b) Radar chart of the 8 QPM techniques.

any QPM, and (ii) draw comparisons between important QPM techniques, as a guide to help the reader find their way in the field of QPM and select the most appropriate technique for their particular application.

Figure 15 visually summarises the results in the form of radar charts, as a means to better compare the features of all the 8 QPM techniques. 9 parameters are included, namely the precision and the trueness (following the results described in Sect. 4), and the simplicity, chromaticity, absolute nature of the measurements, transmission, speed, stability and image definition (following the results described in Sect. 5). Evaluations are made on 3 grades, following the results and the discussion presented in this article. Noteworthy, some of these seven patterns are geometrically nested within others, indicating that certain techniques lack interest compared to others.

It is worth comparing DPM and CGM, which are the two grating-based techniques. The basic version of DPM does not offer clear benefits compared to CGM. The noise of DPM is just better in theory, but in practice it suffers from speckle noise. However, DPM presents interest when accessing Fourier space is necessary, as in this implementation of single-shot, two-color phase measurements [80].

Also, the SLIM pattern is encompassed by the FPM pattern, the two PSI methods based on the use of an SLM, meaning that SLIM does not offer

	Artefacts	Noise	Light source	Implementation	Speed	Stability	Ref.
DHM	No intrinsic artefacts. Fringes coming from the coherence of the laser illumination.	Speckle noise, coming from the coherence of the laser illumination.	Laser	Requires the full modification of a microscope.	Fast	Poor.	[10,11]
CGM	4-fold symmetry when the grating camera distance is too large, typically > 1 mm.	Flicker noise OPD noise < 1 nm	Incoherent Tunable	Easy to implement and use, as it consists of a camera.	Fast	Very good	[13,14]
DPM	Halo and shade-off effects when the pinhole is too large, in particular when using incoherent sources (wDPM).	White noise < 1 nm Higher level with wDPM ~10 nm	Laser or incoherent	Easy to implement as an add-on module on the port of a microscope.	Fast	Very good	[12]
DPC	Halo and shade-off effects	High noise level ~2 nm	Incoherent Tunable	Requires the modification of the illumination	Slower because of the acquisition of 4 images	Very good	[24-25]
PSI	No intrinsic artefacts. Fringes coming from the coherence of the laser illumination.	White noise < 1 nm	Laser	Requires the full modification of a microscope.	Slower because of the acquisition of 4 images	Poor	[15-18]
FPM	Halo and shade-off effects when the phase mask is too large or too small, in particular when using incoherent sources (wDPM).	White noise < 1 nm	Laser or incoherent Not tunable	Easy to implement as an add-on module on the port of a microscope.	Slower because of the acquisition of 4 images	Very good	[19,20]
SLIM	Important halo and shade-off effects.	White noise < 1 nm	Incoherent Not tunable	Easy to implement as an add-on module on the port of a microscope.	Slower because of the acquisition of 4 images	Very good	[21]
TIE	No artefact. Just a loss of spatial resolution for large defocus values.	Flicker noise High noise level ~3 nm	Incoherent. Tunable.	Only requires a standard bright field microscope, with a precise focus adjustment.	Slower because of the acquisition of 3 images	Very good	[22]

DHM Off-axis digital holographic microscopy CGM Cross-grating wavefront microscopy (using QLSI) DPM Diffraction phase microscopy
 DPC differential phase contrast microscopy PSI Phase shifting interferometry microscopy FPM Fourier phase microscopy
 SLIM Spatial light interference microscopy TIE Transport of intensity equation microscopy

Fig. 16 Summary of the main QPM benefits and drawbacks.

significant benefits compared to FPM. It is also not obvious what the interest of SLIM is compared with phase-contrast microscopy, especially for eukaryotic cells. The official interest of SLIM is to turn phase-contrast images into quantitative OPD images. But as demonstrated in this study, images of eukaryotic cells are hardly quantitative in SLIM.

In general, the appropriateness of a method compared to another also depends on the imaged object. For large objects such as eukaryotic cells (neurons, red blood cells, cancer cells, etc), we do not recommend DPC, FPM and SLIM if quantitative dry mass measurements are the aim, because of halo/shade-off effects that tend to underestimate the dry mass.

As a means to summarize the results in a less visual but more detailed manner, Fig. 16 presents a table that includes brief comments on all the features of all the QPM techniques described in this article.

Funding. This project received funding from the European Research Council (ERC) under the European Union’s HORIZON Research and Innovation Programme (proposal number no. 101101026, project MultiPhase).

Data availability. All data required to reproduce the results can be obtained from the corresponding author upon a reasonable request.

Code availability. The Fortran, C++ and Matlab codes used in this study are accessible on the internet:

- The IF-DDA toolbox to compute rigorously the image of an object through a microscope can be downloaded from gitlab [50] or from the webpage:

<https://www.fresnel.fr/spip/spip.php?article2735&lang=fr>

Two codes are available; one where objects are in free space and the other where objects may be in the presence of a multilayer. This is the one used in this article to take the substrate into account.

- The Matlab add-on to the IF-DDA toolbox to implement the QPM configuration is accessible from github [81].

Supplementary Information. The online version contains supplementary material available at <https://xxxxxxxxxxxxxx>.

References

- [1] G. Popescu. *Quantitative phase imaging of cells and tissues*. Mc Graw Hill, 2011.
- [2] K. R. Lee, K. Kim, J. Jung, J. H. Heo, S. Cho, S. Lee, G. Chang, Y. J. Jo, H. Park, and Y. K. Park. Quantitative phase imaging techniques for the study of cell pathophysiology: From principles to applications. *Sensors*, 13:4170–4191, 2013.
- [3] Y. K. Park, C. Depeursinge, and G. Popescu. Quantitative phase imaging in biomedicine. *Nat. Photonics*, 12:578–589, 2018.
- [4] T. Cacace, V. Bianco, and P. Ferraro. Quantitative phase imaging trends in biomedical applications. *Opt. Lasers Eng.*, 135:106188, 2020.
- [5] T. L. Nguyen, S. Pradeep, R. L. Judson-Torres, J. Reed, M. A. Teitell, and T. A. Zangle. Quantitative phase imaging: Recent advances and expanding potential in biomedicine. *ACS Nano*, 16:11516–11544, 2022.
- [6] R. Barer. Interference microscopy and mass determination. *Nature*, 169:366, 1952.
- [7] R. Barer. Refractometry and interferometry of living cells. *J. Opt. Soc. Am.*, 45:545–556, 1957.
- [8] B. Gul, S. Ashraf, S. Khan, H. Nisar, and I. Ahmad. Cell refractive index: Models, insights, applications and future perspectives. *Photodiagnosis Photodyn. Ther.*, 33:102096, 2021.
- [9] T. A. Zangle and Teit. Live-cell mass profiling: an emerging approach in quantitative biophysics. *Nat. Methods*, 11:1221–1228, 2014.
- [10] P. Girshovitz and N. T. Shaked. Generalized cell morphological parameters based on interferometric phase microscopy and their application to cell life cycle characterization. *Biomed. Opt. Express*, 3:1757, 2012.
- [11] P. Marquet, C. Depeursinge, and P. J. Magistretti. Review of quantitative phase-digital holographic microscopy: promising novel imaging technique to resolve neuronal network activity and identify cellular biomarkers of psychiatric disorders. *Neurophotonics*, 1:020901, 2014.
- [12] B. Kemper and G. von Bally. Digital holographic microscopy for live cell applications and technical inspection. *Appl. Opt.*, 47:A52–A61, 2008.
- [13] B. Bhaduri, C. Edwards, H. Pham, R. Zhou, T. H. Nguyen, L. L. Goddard, and G. Popescu. Diffraction phase microscopy:

- principles and applications in materials and life sciences. *Adv. Opt. Photon.*, 6:57–119, 2014.
- [14] Pierre Bon, Guillaume Maucort, Benoit Wattellier, and Serge Monneret. Quadriwave lateral shearing interferometry for quantitative phase microscopy of living cells. *Opt Express*, 17(15):13080–94, 2009.
- [15] G. Baffou. Wavefront microscopy using quadriwave lateral shearing interferometry: from bioimaging to nanophotonics. *ACS Photonics*, 10:322–339, 2023.
- [16] K. Kinnstaetter, A. W. Lohmann, J. Schwider, and N. Streibl. Accuracy of phase shifting interferometry. *Appl. Opt.*, 27:5082–5089, 1988.
- [17] P. de Groot. Principles of interference microscopy for the measurement of surface topography. *Adv. Opt. Photon.*, 7:1–65, 2015.
- [18] D. Zicha and G. A. Dunn. An image processing system for cell behaviour studies in sub-confluent cultures. *J. Microsc.*, 179:11–21, 1995.
- [19] B. Simon, M. Debailleul, V. Georges, V. Lauer, and O. Haeberlé. Tomographic diffractive microscopy of transparent samples. *Eur. Phys. J. Appl. Phys.*, 44:29–35, 2008.
- [20] G. Popescu, L. P. Deflores, J. C. Vaughan, K. Badizadegan, H. Iwai, R. R. Dasari, and M. S. Feld. Fourier phase microscopy for investigation of biological structures and dynamics. *Opt. Lett.*, 29:2503, 2004.
- [21] N. Lue, W. Choi, G. Popescu, T. Ikeda, R. R. Dasari, K. Badizadegan, and M. S. Feld. Quantitative phase imaging of live cells using fast fourier phase microscopy. *Appl. Opt.*, 46:1836–1842, 2007.
- [22] Z. Wang, L. Millet, M. Mustafa, H. Ding, S. Unarunotai, J. Rogers, M. U. Gillette, and G. Popescu. Spatial light interference microscopy (slim). *Opt Express*, 19(2):1016–1026, 2011.
- [23] L. Tia, L. ad Waller. Quantitative differential phase contrast imaging in an led array microscope. *Opt. Express*, 23:11394, 2015.
- [24] M. Chen, L. Tian, and L. Waller. 3d differential phase contrast microscopy. *Biomed. Opt. Express*, 7:3940–3960, 2016.
- [25] A. B. Parthasarathy, K. K. Chu, T. N. Ford, and J. Mertz. Quantitative phase imaging using a partitioned detection aperture. *Opt. Lett.*, 37:4062–4064, 2012.
- [26] L. J. Allen and M. P. Oxley. Phase retrieval from series of images obtained by defocus variation. *Opt. Commun.*, 199:65–75, 2001.
- [27] E. Bélanger, J. P. Bérubé, B. de Dorlodot, P. Marquet, and R. Vallée. Comparative study of quantitative phase imaging techniques for refractometry of optical waveguides. *Opt. Express*, 26:17498–17511, 2018.
- [28] C. Allier, L. Hervé, O. Mandula, P. Blandin, Y. Usson, J. Savatier, S. Monneret, and S. Morales. Quantitative phase imaging of adherent mammalian cells: a comparative study. *Biomed. Opt. Express*, 10:2768–2783, 2019.
- [29] L. Durdevic, A. Relaño Gines, A. Roueff, G. Blivet, and G. Baffou. Biomass measurements of single neurites in vitro using optical wavefront microscopy. *Biomed. Opt. Express*, 13:6550–6560, 2022.
- [30] C. Hu, R. Sam, M. Mingguang, M. Shan, V. Nastasa, M. Wang, T. Kim, M. Gillette, P. Sengupta, and G. Popescu. Optical excitation and detection of neuronal activity. *J. Biophotonics*, 12:e201800269, 2019.
- [31] E. Cuche, P. Marquet, and C. Depeursinge. Simultaneous amplitude-contrast and quantitative phase-contrast microscopy by numerical reconstruction of Fresnel off-axis holograms. *Appl. Opt.*, 38:6994–7001, 1999.
- [32] Ting-Chung Poon and Jung-Ping Liu. *Modern digital holography*. Cambridge University Press, 2014.

- [33] J. Primot and N. Guérineau. Extended hartmann test based on the pseudoguiding property of a hartmann mask completed by a phase chessboard. *Appl. Opt.*, 39(31):5715–5720, 2000.
- [34] J. Primot and N. Guérineau. Achromatic optical interferometer with continuously adjustable sensitivity. *Patent*, page 6577403, 2000.
- [35] G. Baffou. Quantitative phase microscopy using quadriwave lateral shearing interferometry (qlsi): principle, terminology, algorithm and grating shadow description. *J. Phys. D: Appl. Phys.*, 54:294002, 2021.
- [36] G. Baffou. <https://github.com/baffou/cgmprocess>.
- [37] B. C. Platt and R. Shack. History and principles of shack-hartmann wavefront sensing. *J. Refract. Surg.*, 17:S573–S577, 2011.
- [38] Martín-Corral M. and B. Javidi. Fundamentals of 3d imaging and displays: a tutorial on integral imaging, light-field, and plenoptic systems. *Adv. Opt. Photon.*, 10:512–566, 2018.
- [39] V. Bräsiense, J. F. Audibert, T. Wu, G. Tessier, P. Berto, and F. Miomandre. Local surface chemistry dynamically monitored by quantitative phase microscopy. *Small Methods*, 6:2100737, 2022.
- [40] J. Primot. Theoretical description of shack-hartmann wave-front sensor. *Opt. Commun.*, 222:81–92, 2003.
- [41] H. Gong, T. E. Agbana, P. Pozzi, O. Soloviev, M. Verhaegen, and G. Vdovin. Optical path difference microscopy with a shack-hartmann wavefront sensor. *Opt. Lett.*, 42:2122–2125, 2017.
- [42] K. Kim. Single-shot light-field microscopy: An emerging tool for 3d biomedical imaging. *BioChip J.*, 16:397–408, 2022.
- [43] E. R. Polanco, T. E. Moustafa, A. Butterfield, S. D. Scherer, E. Cortes-Sanchez, T. Bodily, B. T. Spike, B. E. Welm, P. S. Bernard, and T. A. Zangle. Multiparametric quantitative phase imaging for real-time, single cell, drug screening in breast cancer. *Commun. Biol.*, 5:794, 2022.
- [44] M. Reed Teague. Deterministic phase retrieval: a green’s function solution. *J. Opt. Soc. Am.*, 73:1434–1441, 1983.
- [45] X. Chen, M. E. Kandel, and G. Popescu. Spatial light interference microscopy: principle and applications to biomedicine. *Adv. Opt. Photon.*, 13(2):353–425, 2021.
- [46] T. H. Nguyen, C. Edwards, L. L. Goddard, and G. Popescu. Quantitative phase imaging with partially coherent illumination. *Opt. Lett.*, 39:5511–5514, 2014.
- [47] B. T. Draine. The discrete-dipole approximation and its application to interstellar graphite grains. *Astrophys. J.*, 333:848–872, 1988.
- [48] P. C. Chaumet. The discrete dipole approximation: A review. *Mathematics*, 10(17), 2022.
- [49] P. C. Chaumet, D. Sentenac, G. Maire, M. Rasedujaman, T. Zhang, and A. Sentenac. Ifdda, an easy-to-use code for simulating the field scattered by 3d inhomogeneous objects in a stratified medium: tutorial. *J. Opt. Soc. Am. A*, 38:1841, 2021.
- [50] P. C. Chaumet. If-ddam toolbox, <https://gitlab.com/ifdda/if-ddam>.
- [51] S. Khadir, D. Andrén, P. C. Chaumet, S. Monneret, N. Bonod, M. Käll, A. Sentenac, and G. Baffou. Full optical characterization of single nanoparticles using quantitative phase imaging. *Optica*, 7:243–248, 2020.
- [52] S. Aknoun, P. Bon, J. Savatier, B. Wattellier, and S. Monneret. Quantitative retardance imaging of biological samples using quadriwave lateral shearing interferometry. *Opt. Express*, 23(12):16383–16406, 2015.
- [53] B. Marthy and G. Baffou. Cross-grating phase microscopy (cgm): In silico experiment

- (insilex) algorithm, noise and accuracy. *Opt. Commun.*, 521:128577, 2022.
- [54] <https://github.com/baffou/cgminsilico>.
- [55] P. Hosseini, R. Zhou, Y. H. Kim, C. Peres, A. Diaspro, C. Kuang, Z. Yaqoob, and P. T. C. So. Pushing phase and amplitude sensitivity limits in interferometric microscopy. *Opt. Lett.*, 41:1656–1659, 2016.
- [56] M. C. Nguyen, P. Bonnaud, R. Dibs, G. Maucort, S. Lonnais, D. Muriaux, and P. Bon. Label-free single nanoparticle identification and characterization including infectious emergent virus. *Small*, page 2304564, 2024.
- [57] S. Khadir, P. Bon, D. Vignaud, E. Galopin, N. McEvoy, D. McCloskey, S. Monneret, and G. Baffou. Optical imaging and characterization of graphene and other 2d materials using quantitative phase microscopy. *ACS Photonics*, 4:3130–3139, 2017.
- [58] V. Bianco, P. Memmolo, M. Leo, S. Montresor, C. Distanto, M. Paturzo, P. Picart, B. Javidi, and P. Ferraro. Strategies for reducing speckle noise in digital holography. *Light Sci. Appl.*, 7:48, 2018.
- [59] J. Reed, J. Chun, T. A. Zangle, S. Kalim, J. S. Hong, S. E. Pefley, X. Zheng, J. K. Gimzewski, and M. A. Teitell. Rapid, massively parallel single-cell drug response measurements via live cell interferometry. *Biophys. J.*, 101:1025–1031, 2011.
- [60] DC. Edwards, B. Bhaduri, T. Nguyen, B. G. Griffin, H. Pham, T. Kim, G. Popescu, and L. L. Goddard. Effects of spatial coherence in diffraction phase microscopy. *Opt. Express*, 22(5133-5146), 2014.
- [61] T. H. Nguyen, C. Edwards, L. L. Goddard, and G. Popescu. Quantitative phase imaging of weakly scattering objects using partially coherent illumination. *Opt. Express*, 24:11683–11693, 2016.
- [62] V. Ayyappan, A. Chang, C. Zhang, S. Kumar Paidi, R. Bordett, T. Liang, I. Barman, and R. Pandey. Identification and staging of b-cell acute lymphoblastic leukemia using quantitative phase imaging and machine learning. *ACS Sensors*, 5:3281–3289, 2020.
- [63] R. Pandey, R. Zhou, R. Bordett, C. Hunter, K. Glunde, I. Barman, T. Valdez, and C. Finck. Integration of diffraction phase microscopy and raman imaging for label-free morpho-molecular assessment of live cells. *J. Biophotonics*, 12:e201800291, 2019.
- [64] X. Gu, L. Lei, Y. Sun, X. Si, M. Wang, F. Li, G. Yang, L. Yang, G. Pan, and W. Huang. Microfluidic diffraction phase microscopy for high-throughput, artifact-free quantitative phase imaging and identification of waterborne parasites. *Opt. Laser Technol.*, 120:105681, 2019.
- [65] T. Ling, K. C. Boyle, V. Zuckerman, T. Flores, C. Ramakrishnan, K. Deisseroth, and D. Palanker. High-speed interferometric imaging reveals dynamics of neuronal deformation during the action potential. *Proc. Natl. Acad. Sci.*, 117:10278–10285, 2020.
- [66] B. Bhaduri, H. Pham, M. Mir, and G. Popescu. Diffraction phase microscopy with white light. *Opt. Lett.*, 37:1094–1096, 2012.
- [67] M. E. Kandel, M. Fanous, C. Best-Popescu, and G. Popescu. Real-time halo correction in phase contrast imaging. *Biomed. Opt. Express*, 9:623–635, 2018.
- [68] K. Zhang, M. Zhu, L. Ma, J. Zhang, and Y. Li. Deep-learning based halo-free white-light diffraction phase imaging. *Front. Phys.*, 9:650108, 2021.
- [69] B. Bhaduri, K. Tangella, and G. Popescu. Fourier phase microscopy with white light. *Biomed. Opt. Express*, 4:1434, 2013.
- [70] T. H. Nguyen, M. Kandel, H. M. Shakir, C. Best-Popescu, J. Arikath, M. N. Do, and G. Popescu. Halo-free phase contrast microscopy. *Sci. Rep.*, 7:44034, 2017.

- [71] C. Zuo, J. Li, J. Su, Y. Fan, J. Zhang, L. Lu, R. Zhang, B. Wang, L. Huang, and Q. Chen. Transport of intensity equation: a tutorial. *Opt. Lasers Eng.*, 135:106187, 2020.
- [72] A. Descloux, K. S. Grussmayer, E. Bostan, T. Lukes, A. Bouwens, A. Sharipov, S. Geissbuehler, A. L. Mahul-Mellier, H. A. Lashuel, M. Leutenegger, and T. Lasser. Combined multi-plane phase retrieval and super-resolution optical fluctuation imaging for 4d cell microscopy. *Nature Photon.*, 12:165–172, 2018.
- [73] Y. Choi, T. D. Yang, K. J. Lee, and W. Choi. Full-field and single-shot quantitative phase microscopy using dynamic speckle illumination. *Opt. Lett.*, 36:2465–2467, 2011.
- [74] S. Aknoun, J. Savatier, P. Bon, F. Galland, L. Abdeladim, B. Wattellier, and S. Monneret. Living cell dry mass measurement using quantitative phase imaging with quadriwave lateral shearing interferometry: an accuracy and sensitivity discussion. *J. Biomed. Opt.*, 20(12):126009, 2015.
- [75] M. Bénéfice, A. Gorlas, B. Marthy, V. Da Cunha, P. Forterre, A. Sentenac, P. C. Chaumet, and G. Baffou. Dry mass photometry of single bacteria using quantitative wavefront microscopy. *Biophys. J.*, 122:1–14, 2023.
- [76] S. Aknoun, M. Aurrand-Lions, B. Wattellier, and S. Monneret. Quantitative retardance imaging by means of quadri-wave lateral shearing interferometry for label-free fiber imaging in tissues. *Opt. Commun.*, 422:17–27, 2018.
- [77] V. K. Lam, T. Phan, K. Ly, X. Luo, G. Nehmetallah, and C. B. Raub. Dual-modality digital holographic and polarization microscope to quantify phase and birefringence signals in biospecimens with a complex microstructure. *Biomed. Opt. Express*, 13:805–823, 2022.
- [78] P. Bon, S. Lécart, E. Fort, and S. Lévêque-Fort. Fast label-free cytoskeletal network imaging in living mammalian cells. *Biophys. J.*, 106:1588–1595, 2014.
- [79] Sánchez-Ortiga E., A. Doblas, M. Martínez-Corral, and J. Garcia-Sucerquia. Off-axis digital holographic microscopy: practical design parameters for operating at diffraction limit. *Appl. Opt.*, 53:2058–2066, 2014.
- [80] P. Hosseini, D. Jin, Z. Yaqoob, and P. T. C. So. Single-shot dual-wavelength interferometric microscopy. *Methods*, 136:35–39, 2018.
- [81] G. Baffou. <https://github.com/baffou/cgm-qpm>.